

Warm Ionized Gas Outflows in Active Galactic Nuclei: What Causes it?

PAYEL NANDI ^{1,2} C.S. STALIN ¹ AND D.J.SAIKIA ³

¹*Indian Institute of Astrophysics, Block II, Koramangala, Bangalore, 560034, India*

²*Joint Astronomy Programme, Department of Physics, Indian Institute of Science, Bangalore, 560012, India*

³*Inter-University Centre for Astronomy and Astrophysics, IUCAA, Pune 411007, India*

ABSTRACT

The driving force behind outflows, often invoked to understand the correlation between the supermassive black holes powering active galactic nuclei (AGN) and their host galaxy properties, remains uncertain. We provide new insights into the mechanisms that trigger warm ionized outflows in AGN, based on findings from the MaNGA survey. Our sample comprises 538 AGN with strong [OIII] $\lambda 5007$ emission lines, of which 197 are detected in radio and 341 are radio-undetected. We analyzed [OIII] $\lambda 5007$ line in summed spectra, extracted over their central 500×500 pc² region. The calculated Balmer 4000 Å break, $D_n 4000$ is larger than 1.45 for $\sim 95\%$ of the sources indicating that the specific star-formation rate in their central regions is smaller than $10^{-11.5}$ yr⁻¹, pointing to evidence of negative AGN feedback suppressing star-formation. Considering the whole sample, radio-detected sources show an increased outflow detection rate ($56 \pm 7\%$) compared to radio-undetected sources ($25 \pm 3\%$). They also show higher velocity, mass outflow rate, outflow power and outflow momentum rate. We noticed a strong correlation between outflow characteristics and bolometric luminosity in both samples, except that the correlation is steeper for the radio-detected sample. Our findings suggest (a) warm ionized outflows are prevalent in all types of AGN, (b) radiation from AGN is the primary driver of these outflows, (c) radio jets are likely to play a secondary role in enhancing the gas kinematics over and above that caused by radiation, and (d) very low star-formation in the central regions of the galaxies, possibly due to negative feedback of AGN activity.

Keywords: Active galactic nuclei (16) — Seyfert galaxies (1447) — LINER galaxies (925) — radio jets (1347) — AGN host galaxies (2017)

1. INTRODUCTION

Supermassive black holes (SMBHs) with masses (M_{BH}) greater than $10^6 M_\odot$ are generally known to reside at the centres of all massive galaxies in the Universe (Martín-Navarro et al. 2018; and references therein). A small fraction of these galaxies hosts active galactic nuclei (AGN) caused by the accretion of matter from the surroundings by these SMBHs (Padovani et al. 2017), though less common in dwarf galaxies that host intermediate-mass black holes with $M_{BH} < 10^6 M_\odot$ (Reines 2022). The process of accretion which leads to the release of enormous amounts of energy in the form of radiation (Lynden-Bell 1969) as well as particles via

relativistic jets (Cattaneo & Best 2009) is believed to affect their host galaxies via a process called feedback. AGN feedback is invoked to explain the observed correlation between M_{BH} and various host galaxy properties (Zhuang & Ho 2023 and references therein).

A viable feedback mechanism in AGN is outflows. These outflows are dynamic phenomena, representing the expulsion of vast amounts of matter and energy from the vicinity of SMBHs at the centres of galaxies. They play a crucial role in shaping the surrounding environment and influencing the evolution of galaxies (Guo et al. 2023). They are multifaceted, as seen in molecular, neutral and ionized gas (Nandi et al. 2023b; Riffel et al. 2023; Su et al. 2023; Izumi et al. 2023) and can occur on various scales, spanning from relatively small-scale winds to colossal jets extending over intergalactic distances (Harrison et al. 2014; Nandi et al. 2023b; Izumi et al. 2023; Guo et al. 2023; Saikia 2022, for a review).

They can profoundly impact the galaxy’s evolution by regulating the rate of star formation, distributing elements crucial for planetary systems, and even influencing the growth of SMBHs (Nandi et al. 2023a; Venturi et al. 2023; Nandi et al. 2024). Irrespective of outflows being prevalent in AGN, questions such as (a) what drives these outflows and (b) at what scales they operate are not conclusively known and are highly debated. The potential mechanisms that could drive these outflows could be radiation and/or radio jets (Wylezalek & Morganti 2018).

Studies are available in the literature aimed at identifying the main driving mechanisms for outflows. They are focused on individual systems as well as on a sample of sources. For example, the correlation noticed between the ionized [OIII] λ 5007 gas outflow and the radio jet in NGC 1068, seems to favour a jet driven outflow (García-Burillo et al. 2014; Venturi et al. 2021). In IC 5063, Morganti et al. (2015) found evidence of molecular, atomic and ionized outflows and conclude that both the radiation and jet could drive the outflow, however, the jet being the dominant driver. Other studies that find favour of jets triggering outflows include that of NGC 1337 (Aalto et al. 2016), a sample of 10 quasars at $z < 0.2$ (Jarvis et al. 2019), 3C 273 (Husemann et al. 2019), ESO 420–G13 (Fernández-Ontiveros et al. 2020), NGC 5643 (Venturi et al. 2021), NGC 1386 (Venturi et al. 2021), J1316+1753 (Girdhar et al. 2022), B2 0258+35 (Murthy et al. 2022), N0945+1737 (Speranza et al. 2022), the Teacup galaxy (Audibert et al. 2023) and the dwarf AGN NGC 4395 (Nandi et al. 2023b). However, observations of Mrk 231 support radiation from accretion driving the outflow (Feruglio et al. 2015). While the above studies are focused on using high-resolution observations, low spatial resolution studies do exist. Mullaney et al. (2013) from analysis of a larger sample of quasars using the Sloan Digital Sky Survey (SDSS)¹ spectra, found that sources more luminous in radio band tend to have broader [OIII] λ 5007 line profile, while, Zakamska & Greene (2014) found favour of outflows being driven via radiative output from quasars. From an analysis of SDSS spectra of Type 2 AGN, Woo et al. (2016) found that while outflows are prevalent in Type 2 AGN, they are not directly related to radio activity. Alternatively, from an analysis of the SDSS spectra of radio AGN, Kukreti et al. (2023) found that radio jets are more effective in driving outflows when they are young. Molyneux et al. (2019) too found that the chance of finding outflows is more in compact radio sources possibly

hosting young radio jets. Recently, from an analysis of a large sample of AGN, Liao et al. (2024) found the outflow velocity to correlate with radio power. However, Ayubinia et al. (2023), conclude, that both accretion and radio activity can have a role in driving outflows.

These studies aimed at finding the driver of outflows, have focussed on both radio-loud and radio-quiet quasars. This is misleading as even radio-quiet quasars are found to have radio jets that could impact the outflow. Also, the separation of quasars into radio-loud and radio-quiet is questioned, and an alternative division of AGN into jetted and non-jetted sources is proposed (Padovani 2017). Thus, the driver for outflows in AGN remains unsettled. To overcome the above limitations, firstly, we utilised in this work a sample of AGN separated into radio-detected and radio-undetected. This inclusion of radio-undetected sources makes sure that these sources lack clear signatures of radio jets (considering that the radio emission in radio-detected AGN is due to jets in them and not due to star formation in their hosts) at the sensitivity levels of existing radio surveys. And, secondly, we used spatially resolved spectroscopic data on a large sample of AGN hitherto not utilised for such a comparative study.

2. SAMPLE

Our initial sample of sources was derived from the MaNGA (Mapping Nearby Galaxies at Apache Point Observatory; Bundy et al. 2015) survey, a spectroscopic program under SDSS-IV. MaNGA employs a fiber-based integral field unit (IFU) spectroscopic technique, utilizing the two BOSS spectrographs mounted on the 2.5-meter Sloan Foundation Telescope at Apache Point Observatory. MaNGA has observed 10,010 unique galaxies with redshifts ranging from 0.01 to 0.15 (Wake et al. 2017), using different IFU configurations. The spatial resolution achieved is between $2''$ and $2.5''$, with a spectral resolution of approximately 2000. The program’s field of view varies from $12''$ to $32''$, depending on the IFU configuration, covering a spatial range of 1.5 to 2.5 effective radii of the observed galaxies. We cross-correlated the sources in the MaNGA catalogue (Wake et al. 2017) with the latest version of the Million Quasars Catalogue (MILLIQUAS; Flesch 2023) to identify genuine AGN in the MaNGA catalogue, using a search radius of $2''$. MILLIQUAS is a collection of all published AGN and quasars till 30 June 2023, amounting to a total of 1,021,800 sources. Our cross-correlation of MaNGA sources with MILLIQUAS led to a sample of 1,142 AGN. As these sources were pulled from various surveys in MILLIQUAS, we checked the position of these 1142 sources in the Baldwin-Phillips-

¹ <https://sdss.org/>

Terlevich diagram (BPT; Baldwin et al. 1981) for homogeneity. We took an aperture of 500×500 square pc box centred on the source and calculated the flux values of [OIII] $\lambda 5007$, H β , H α , [NII] $\lambda 6584$, [SII] $\lambda 6718$ and [SII] $\lambda 6732$ lines from the Data Analysis Pipeline (DAP) products (Westfall et al. 2019) of MaNGA. Then, we plotted the flux ratio between [OIII] $\lambda 5007$ and H β , [SII] $\lambda(6717+6732)$ and H α and also the flux ratio between [OIII] $\lambda 5007$ and H β , [NII] $\lambda 6584$ and H α in for the sources in the BPT diagrams. Then, out of these 1142 sources, 718 are above the star-forming line in the [SII] $\lambda(6717+6732)$ /H α vs [OIII] $\lambda 5007$ /H β diagram and 740 sources lie above the star formation line in the [NII] $\lambda 6584$ /H α vs [OIII] $\lambda 5007$ /H β diagram with 688 common sources in both the BPT diagrams. We considered these 688 AGN for our analysis out of which 252 are Seyferts, and 436 are LINERs.

We cross-matched these 688 AGN with the VLA Faint Images of the Radio Sky at Twenty-Centimeters (FIRST) survey (Becker et al. 1995) using an angular separation of $3''$. The FIRST survey, conducted with the NRAO Very Large Array in its B-configuration, provides radio maps of the sky at 20 cm (1.4 GHz) with a beam size of approximately $5.4''$, a typical root mean square (rms) noise level of $0.14 \text{ mJy beam}^{-1}$. Through this cross-matching process, we identified 217 AGN with radio counterparts in the FIRST catalogue, exhibiting flux densities greater than 0.5 mJy , classifying them as radio-detected. The remaining 471 AGN, lacking radio counterparts in the FIRST survey, were categorized as radio-undetected. Out of these 471 sources, 18 sources are not covered by the FIRST survey. Not considering those 18 sources, our final radio-undetected sample consists of 453 sources. Of the 217 radio-detected sample 95 sources are Seyfert type AGN while 122 are LINERs. Similarly, among the 453 radio-undetected sample, 149 sources are Seyfert type AGN while 304 sources are LINERs. The positions of these sources in the BPT diagrams are shown in Appendix A (see Fig. A1). Both the radio-detected and the radio-undetected samples have similar distributions in the redshift and optical B-band brightness plane (see Fig. A2). A Kolmogorov-Smirnov (KS) test carried out on their distributions of redshift and B-band brightness indicates that the two samples are indeed indistinguishable with statistics of 0.07 and a p-value of 0.12.

3. ANALYSIS

We focussed our analysis on a total of 217 AGN with radio detection and 453 AGN without radio detection in the FIRST survey. For this, we used the data reduction pipeline (DRP) products (Law et al. 2016) LOGCUBE

of SDSS DR17. The DRP products contain the processed, and calibrated spectra for each spaxel in the field of view in form of cube for each source.

For each of the sources studied in this work, we generated summed spectra in the rest frame of the sources over a square with the length of the side of 500 pc. The choice of 500 pc is due to our requirement of having at least one spaxel to generate the spectra for most of the sources.

We fitted the [OIII] $\lambda 5007$ profile with multiple Gaussian components along with a first-order polynomial for the continuum using the nonlinear least square fitting algorithm within the *curvefit* module in the *Scipy* library. We fitted [OIII] $\lambda 5007$ because we are only interested in the warm ionised phase of outflow that is traced by the forbidden bright line [OIII] $\lambda 5007$. During the fit, we kept the width, peak and amplitude of each of the components as free parameters. Also, we restricted the fitting to those sources for which the signal-to-noise ratio (SNR) of the line is more than 3.0. Here, SNR refers to the ratio of the flux at the peak of the line to the standard deviation of continuum fluxes on either side of the line. We used a total of 80 \AA width for the spectral region ($4977\text{--}5057 \text{ \AA}$) during the fitting. For some sources, the [OIII] $\lambda 5007$ line profile was adequately modelled with a single Gaussian component. However, in cases where the residual, defined as $(\text{data} - \text{model})/\text{data}$, exceeded 10%, additional Gaussian components were considered. The residual was reassessed after each addition and compared to the previous fit. If including an additional Gaussian reduced the residual and smoothed fluctuations in both the surrounding continuum and the line region, the extra component was adopted. Otherwise, the fit was restricted to the minimum number of Gaussian components required. For cases where more than one Gaussian component was necessary, an additional criterion was applied: the peak of the second and third components have to exceed three times the standard deviation of the continuum fluxes to confirm their statistical significance. In the radio-detected sample, the SNR of the first outflow component ranges from 10 to 306, while the SNR of the second outflow component ranges from 8 to 331. In the radio-undetected sample, the SNR of the first outflow component ranges from 4 to 199, and the SNR of the second outflow component ranges from 3 to 122. We show in Fig. A3, the spectral fits to three sources, one requiring a single Gaussian component, while the others requiring two and three Gaussian components, respectively. We also manually inspected each of the fitted spectra to ensure their fitting was correct.

After the fitting, we corrected the measured outflow fluxes for galactic extinction using Cardelli et al. (1989) and the $E(B-V)$ values given in the header of DRP files. The fluxes were also corrected for internal extinction using the $H\alpha$ and $H\beta$ ratio taken from DAP products and following Miller & Mathews (1972); Veilleux et al. (1995) and Calzetti et al. (2000). Under the theoretical assumption of case B recombination, the intrinsic $H\alpha/H\beta$ ratio was taken as 3.1 (Osterbrock & Ferland 2006).

4. RESULTS AND DISCUSSION

4.1. Detection of outflows

For both the radio-detected and the radio-undetected samples, we searched for the signature of outflows over a region of 500×500 square pc centered on each of the sources. The $[OIII]\lambda 5007$ line was detected at the 3σ limit for 197 sources in the radio-detected category and 341 sources in the radio-undetected category. Our final sample thus consists of a total of 538 sources with strong $[OIII]\lambda 5007$ for further analysis.

For the radio-detected sample, out of 197 sources, for 86 sources, a single Gaussian component proved sufficient for fitting the $[OIII]\lambda 5007$ line, for 77 sources, two Gaussian components were needed to fit the line, while for 34 sources three Gaussian components were needed to model the line. Considering sources that require more than one Gaussian component to well represent the $[OIII]\lambda 5007$ line, in the radio-detected category, a total of 111 out of 197 sources ($56 \pm 7\%$), prominently showed discernible signatures indicative of outflows.

Similarly, in the radio-undetected sample, out of the 341 sources, 257 sources required a single Gaussian component to well represent the $[OIII]\lambda 5007$ line, while 69 sources required two Gaussian components and 15 sources needed three Gaussian components to well model the line. Thus, in the radio-undetected sample, we detected outflows for 84 sources i.e. $25 \pm 3\%$ of the sources showed signatures of outflows. This clearly indicates that the outflow detection rate is higher in the radio-detected sample compared to the radio-undetected sample.

We also classified our sample into Seyferts and LINERs based on their location in the BPT diagram (Fig. A1) to investigate their prevalence of outflows. In the radio-detected sample, we have 92 Seyferts and 105 LINERs for which $[OIII]\lambda 5007$ was significantly detected. Of these, we detected outflows in 81 Seyferts and 30 LINERs. Similarly, in the radio-undetected sample, we detected $[OIII]\lambda 5007$ line in 131 Seyferts and 210 LINERs. Of these, we detected outflows in 66 Seyferts and

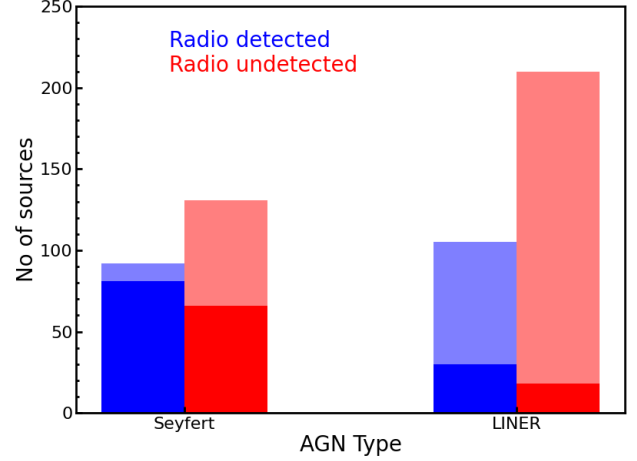


Figure 1. Bar chart of the different types of AGN (Seyferts and LINERs) used in this study. Here, the large blue bar refers to the total radio-detected sources, and the large red bar refers to the total radio-undetected sources. Dark-shaded regions refer to outflow-detected sources.

18 LINERs. The results of the analysis are summarised in Table 1 and in Fig. 1.

Considering the total sample, we found that $66 \pm 7\%$ of Seyferts show outflows, compared to only $15 \pm 2\%$ LINERs. In radio-detected Seyferts, outflows are detected in $88 \pm 13\%$ sources, while in radio-detected LINERs, it is $29 \pm 6\%$. In the case of the radio-undetected sample, we detected outflows for $50 \pm 8\%$ Seyferts and $8 \pm 2\%$ LINERs. Thus Seyferts consistently show more frequent outflows than LINERs, both in radio-detected and radio-undetected samples. This is in agreement with a recent study by Torres-Papaqui et al. (2024) who, too, from a systematic analysis of the SDSS spectra of a large sample of Seyferts and LINERs, found that the probability of detecting outflows in LINERs is lower compared to that of Seyferts.

4.2. Comparison of kinematics properties of outflow

In the following sections, we compared the kinematic properties of outflow in our sample of sources. In cases where two outflowing components were detected, we initially consider only the brightest of the two in the analysis of the kinematic properties of the outflow. We later also considered the outflowing component of lower brightness, and also the one with the higher velocity. The values for the brighter component are tabulated in Table 2 for the total sample, the Seyferts and LINERs and among them separately into radio-detected and radio-undetected samples. Similar Tables for the other two cases are given in the Appendix B.

4.2.1. Velocity shift

Table 1. Summary of the sources analysed for ionised outflows in the [OIII] λ 5007 line.

	Total Sample		radio-detected			radio-undetected		
	Seyferts	LINERs	Total	Seyferts	LINERs	Total	Seyferts	LINERs
Total number of sources	223	315	197	92	105	341	131	210
Number of source with one Gaussian component	76	267	86	11	75	257	65	192
Number of sources with two Gaussian components	99	47	77	47	30	69	52	17
Number of sources with three Gaussian components	48	1	34	34	0	15	14	1
Number of sources with outflow	147	48	111	81	30	84	66	18
Outflow detection rate in percentage	66 \pm 7	15 \pm 2	56 \pm 7	88 \pm 13	29 \pm 6	25 \pm 3	50 \pm 8	8 \pm 2

We measured the velocity shift (V_{shift}) of the outflowing component relative to the narrow component of the [OIII] λ 5007 emission line. In this definition, a negative value of V_{shift} corresponds to the broad blueshifted component and a positive value of V_{shift} corresponds to the broad redshifted component. The distribution of V_{shift} for both the radio-detected and radio-undetected sample of sources is shown in the upper left panel of Fig. 2. The KS test reveals that the distributions of the two samples are not statistically different, with a p-value of 0.4. For the radio-detected sample, V_{shift} ranges from -782 km s^{-1} to 463 km s^{-1} , with a mean of -178 km s^{-1} and a median of -163 km s^{-1} with median uncertainty of 46 km s^{-1} . Similarly for the radio-undetected sample, V_{shift} ranges from -628 km s^{-1} to 108 km s^{-1} , with a mean of -234 km s^{-1} and a median of -167 km s^{-1} with median uncertainty of 70 km s^{-1} . In both our samples, we found more sources ($\sim 80\%$) to show blue asymmetries of their [OIII] λ 5007 line relative to red asymmetry. This could be because of the redshifted part of the bipolar outflow being obscured by dust and/or seen at a lower S/N than the blue-shifted component and thus undetected (Belli et al. 2024).

4.2.2. Velocity dispersion

We parameterise the emission line profile of the outflowing component using the dispersion of the line parameter ($\sigma_{measured}$) obtained from the fitting of the [OIII] λ 5007 line. This measured velocity dispersion of the outflowing component, $\sigma_{measured}^2 = \sigma_{out}^2 + \sigma_{inst}^2$, where σ_{out} and σ_{inst} are the intrinsic velocity dispersion of the outflowing component and the dispersion of the instrumental line spread function. For MaNGA, the 1σ width of the instrumental line spread function is $\sim 70 \text{ km s}^{-1}$ (Law et al. 2022). To estimate σ_{out} , we subtracted σ_{inst} from $\sigma_{measured}$ in quadrature. From the estimated σ_{out} , we calculated the full width at half maximum (FWHM) of the outflowing component as $FWHM_{out} = 2\sqrt{2\ln 2} \sigma_{out} = 2.35\sigma_{out}$, which is valid for a true Gaussian profile. The distribution of $FWHM_{out}$

is shown in the upper middle panel of Fig. 2 for both the radio-detected and radio-undetected samples.

For the radio-detected category, $FWHM_{out}$ ranges from 169 km s^{-1} to 1398 km s^{-1} , with a mean value of 646 km s^{-1} and a median of 626 km s^{-1} with median uncertainty of 59 km s^{-1} . For the radio-undetected category, $FWHM_{out}$ ranges from 140 km s^{-1} to 1171 km s^{-1} and it is lower compared to radio-detected sample, with a mean of 526 km s^{-1} and a median of 518 km s^{-1} along with median uncertainty of 82 km s^{-1} . Therefore, this larger range and higher values of $FWHM_{out}$ for radio-detected sources indicate that the outflowing material in them is more kinematically disturbed compared to radio-undetected sources.

4.2.3. Outflow velocity

We define the outflow velocity, V_{out} , as the sum of the velocity difference ($|V_{shift}|$) between the outflowing component and the narrow component, plus two times the standard deviation of the outflowing component (σ_{out}), i.e., $V_{out} = |V_{shift}| + 2\sigma_{out}$ (Parlanti et al. 2024). The distribution of V_{out} is shown in the upper right panel of Fig. 2 for both the radio-detected and radio-undetected samples. The KS test indicates that the distributions of the radio-detected and radio-undetected populations are statistically distinct, with a p-value of 6×10^{-3} . This low p-value suggests that the likelihood of these two distributions being drawn from the same parent population is very low.

For the radio-detected sample, the outflow velocity V_{out} spans from 271 km s^{-1} to 1970 km s^{-1} , with an average velocity of 788 km s^{-1} and a median velocity of 705 km s^{-1} with median uncertainty of 74 km s^{-1} . In contrast, the radio-undetected sources exhibit a range of V_{out} from 118 km s^{-1} to 1387 km s^{-1} , with a lower mean velocity of 691 km s^{-1} and a median of 610 km s^{-1} along with median uncertainty of 98 km s^{-1} . The higher velocities in the radio-detected sample may imply that radio emission is linked to more powerful or sustained outflows, possibly associated with jet-driven mechanisms or enhanced AGN activity. The contrast

in median and mean velocities between the two samples supports the idea of a significant difference in outflow dynamics related to the presence of radio emission.

4.2.4. Asymmetric index

To evaluate the asymmetry of the total [OIII] λ 5007 line profile, we utilize the asymmetry index (AI). Following Zakamska & Greene (2014), the AI is defined as

$$AI = \frac{(V95 - V50) - (V50 - V05)}{V95 - V05} \quad (1)$$

Here V95, V50 and V05 are the velocities at which 95%, 50% and 5% of the emission line flux is found. A value of zero indicates a symmetric profile, a positive value suggests redshifted wings, and a negative value indicates blueshifted wings. The middle left panel of Fig. 2 displays the distribution of AI values for both the radio-detected and radio-undetected samples. Statistically, these distributions differ, with a KS test statistic of 0.32 and a p-value of 0.04, suggesting a significant but moderate distinction between the two groups.

For the radio-detected sample, AI values range from -0.46 to 0.12 , with an average of -0.15 and a median of -0.16 with median uncertainty of 0.05 . In contrast, the radio-undetected sample has a wider range from -0.51 to 0.16 , with a mean value of -0.18 and a median of -0.17 with median uncertainty of 0.10 . The consistently negative AI in both the samples suggests the dominance of the blueshifted component of the bipolar outflow relative to the redshifted component of the outflow, as discussed in section 4.2.1.

4.2.5. Outflow mass

We determined the mass of the outflowing gas (M_{out}) following Carniani et al. (2024) as

$$M_{out} = 0.8 \times 10^8 \left(\frac{L_{[OIII]out}}{10^{44} \text{ erg s}^{-1}} \right) \left(\frac{500 \text{ cm}^{-3}}{n_e} \right) \left(\frac{Z_{\odot}}{Z} \right) M_{\odot} \quad (2)$$

Here, $L_{[OIII]out}$ is the luminosity of the outflowing component calculated from the flux of the outflowing component of [OIII] λ 5007 and corrected for dust extinction following the procedure given in Section 3. The outflow mass also depends on both the electron density (n_e) and the gas phase metallicity of the medium. We calculated n_e using the ratio of [SII] λ 6718 to [SII] λ 6732, assuming an electron temperature of 10,000 K, using *pyneb* (Luridiana et al. 2015). We also determined the gas phase metallicity using [OIII] λ 4959,5007, [NII] λ 6548,6584, and the Balmer lines ($H\alpha$ and $H\beta$), as described by do Nascimento et al. (2022).

The distribution of M_{out} for both the radio-detected and radio-undetected samples is illustrated in the middle panel of Fig. 2. A KS test shows that the two distributions are statistically distinct, with a p-value of 6×10^{-4} . For the radio-detected sample, M_{out} ranges from $181 M_{\odot}$ to $2.4 \times 10^6 M_{\odot}$, with a mean of $1.1 \times 10^5 M_{\odot}$ and a median of $3.5 \times 10^4 M_{\odot}$ with median uncertainty of $1.4 \times 10^3 M_{\odot}$. In contrast, the radio-undetected sample, shows M_{out} values ranging from $30 M_{\odot}$ to $1.5 \times 10^5 M_{\odot}$, with a mean of $2.5 \times 10^4 M_{\odot}$ and a median of $9.6 \times 10^3 M_{\odot}$ along with median uncertainty of $8.6 \times 10^2 M_{\odot}$. This finding suggests that outflow masses are notably higher in radio-detected sources than in radio-undetected sources.

4.2.6. Mass outflow rate

We calculated the mass outflow rate (\dot{M}_{out}), which represents the mass of gas outflowing per unit time as

$$\dot{M}_{out} = \frac{V_{out} M_{out}}{R} \quad (3)$$

We considered R as 500 pc. The distribution of \dot{M}_{out} for both the radio-detected and radio-undetected samples is illustrated in the middle right panel of Fig. 2. According to the KS test, the distributions differ significantly, with a p-value of 5×10^{-5} . For the radio-detected sample, \dot{M}_{out} ranges from 2.3×10^{-4} to $5.1 M_{\odot} \text{ yr}^{-1}$, with a mean of $0.17 M_{\odot} \text{ yr}^{-1}$ and a median of $0.04 M_{\odot} \text{ yr}^{-1}$ with median uncertainty of $0.004 M_{\odot} \text{ yr}^{-1}$. For the radio-undetected sample, \dot{M}_{out} ranges from 8.0×10^{-5} to $0.2 M_{\odot} \text{ yr}^{-1}$, with a mean of $0.03 M_{\odot} \text{ yr}^{-1}$ and a median of $0.01 M_{\odot} \text{ yr}^{-1}$ with median uncertainty of $0.002 M_{\odot} \text{ yr}^{-1}$. These results indicate that \dot{M}_{out} is consistently higher in radio-detected sources compared to radio-undetected ones.

4.2.7. Power of outflows

The kinetic power of outflows (KP_{out}) is defined as

$$KP_{out} = \frac{1}{2} \dot{M}_{out} V_{out}^2 \quad (4)$$

The distribution of KP_{out} for our sample of sources is shown in the bottom left panel of Fig. 2. The figure shows that radio-detected sources exhibit more powerful outflows than radio-undetected sources. From KS test, we found that the distributions of KP_{out} for the radio-detected and radio-undetected samples are indeed different with a p-value of 2×10^{-7} .

For the radio-detected sample, KP_{out} ranges from 2.0×10^{37} to $1.8 \times 10^{42} \text{ erg s}^{-1}$, with a mean of $4.6 \times 10^{40} \text{ erg s}^{-1}$ and a median of $4.8 \times 10^{39} \text{ erg s}^{-1}$ with median uncertainty of $1.8 \times 10^{39} \text{ erg s}^{-1}$. In the radio-undetected sample, KP_{out} varies from 3.3×10^{37} to

$7.0 \times 10^{40} \text{ erg s}^{-1}$, with a mean of $4.2 \times 10^{39} \text{ erg s}^{-1}$ and a median of $1.3 \times 10^{39} \text{ erg s}^{-1}$ with median uncertainty of $5.9 \times 10^{38} \text{ erg s}^{-1}$.

This indicates that radio-detected sources consistently exhibit higher outflow power compared to radio-undetected sources. This difference could suggest that radio emission is likely associated with more energetic outflows, possibly jets, potentially amplifying the AGN's feedback impact on the surrounding gas. Higher outflow power in radio-detected galaxies may be a sign of more efficient energy transfer from the AGN to the host galaxy's interstellar medium, possibly affecting star formation and the overall galactic environment (King & Pounds 2015).

4.2.8. Momentum rate of outflows

The momentum rate of outflows (\dot{P}_{out}) is defined as $\dot{P}_{out} = \dot{M}_{out} V_{out}$. The distribution of \dot{P}_{out} (outflow momentum rate) for the sample is shown in the bottom middle panel of Fig. 2. According to the KS test, \dot{P}_{out} is significantly higher in radio-detected sources than in radio-undetected ones, with a p-value of 9×10^{-7} .

For radio-detected sources, \dot{P}_{out} spans from 8.3×10^{29} to $3.4 \times 10^{34} \text{ g cm s}^{-2}$, with a mean of $9.2 \times 10^{32} \text{ g cm s}^{-2}$ and a median of $1.7 \times 10^{32} \text{ g cm s}^{-2}$ with median uncertainty of $3.0 \times 10^{31} \text{ g cm s}^{-2}$. For the radio-undetected sources, \dot{P}_{out} ranges from 5.8×10^{29} to $1.2 \times 10^{33} \text{ g cm s}^{-2}$, with a mean of $1.1 \times 10^{32} \text{ g cm s}^{-2}$ and a median of $5.1 \times 10^{31} \text{ g cm s}^{-2}$ and with median uncertainty of $1.5 \times 10^{31} \text{ g cm s}^{-2}$. This indicates that \dot{P}_{out} is nearly an order of magnitude higher in radio-detected sources compared to radio-undetected sources.

The elevated \dot{P}_{out} in radio-detected sources suggests a stronger coupling between the AGN energy and the outflow momentum, enhancing feedback effects on the host galaxy. Given the higher outflow power (KP_{out}) and mass outflow rates (\dot{M}_{out}) in these sources, it appears that radio activity is correlated with more efficient AGN feedback. This combination of higher momentum, power, and mass flow may drive larger-scale gas movements, which could potentially lead to star formation suppression or triggering in the host galaxy more effectively than in radio-undetected sources (Fabian 2012; King & Pounds 2015; Tadhunter 2016).

We have so far focused on the brightest outflowing component in this Section 4.2 when multiple components were detected. This approach may lead to an over representation of highly ionized outflows while potentially underestimating those with higher velocities but lower ionization. To assess this potential bias, we conducted two additional analyses: one considering the less

luminous outflows and another focusing on the outflows with higher velocities. The results of these analyses are provided in Appendix B (Tables B1, B2). Across all cases, we observed that radio-detected sources consistently exhibit higher velocities, mass outflow rates, outflow powers, and outflow momentum rates compared to their radio-undetected counterparts.

4.3. Outflows in Seyferts vs LINERs

From Tables 2, B1 and B2, it is evident that the FWHM_{out} and V_{out} are significantly greater in LINERs relative to Seyferts, suggesting higher outflow velocities in them. Additionally, a comparison of V_{shift} reveals that the outflows are more blueshifted in LINERs than Seyferts. This larger velocity structure in LINERs may be linked to shock-dominated emission, as suggested by Dopita & Sutherland (1995). However, when considering the mass outflow rate, outflow power and outflow momentum rate, Seyferts exhibit notably higher values, along with a greater outflow detection rate, as discussed in Section 4.1. This contrast is likely due to LINERs being at the low luminosity end of AGN, with ionizing power and accretion rate lower than that of Seyferts (Heckman 1980; Ho 2008; Márquez et al. 2017), producing less outflowing material, thereby resulting in lower detection rates and less powerful outflows.

4.4. Infrared properties of outflows

Of the sources analysed in this work, more than half of them are found to show outflows, as evidenced by the presence of shifted broad asymmetric wings in their [OIII] λ 5007 line. Such observed line profile could be the result of gas outflows from the central region of these sources (Zamanov et al. 2002). Such outflows can also be from the inner narrow line region (NLR) related to the winds from AGN (Elvis 2000). Alternatively, outflows can also be driven by star formation processes via winds from massive stars and/or Type 2 supernova explosions (Parlanti et al. 2024). Studies available in the literature point to infrared observations being an effective tool to distinguish between these two processes, namely AGN driven and star formation driven outflows. Therefore, to investigate the infrared properties of the sources with outflows, we cross-correlated our sources with the *Wide-field Infrared Survey Explorer* (WISE; Wright et al. 2010) catalog² using a search radius of 3 arcsec for both our samples. To ensure reliable data for analysis, we only included sources with a signal-to-noise ratio (SNR) greater than 3.0 in the W3 band. Since the WISE catalogue provides magnitudes in the Vega system by de-

² <https://irsa.ipac.caltech.edu/Missions/wise.html>

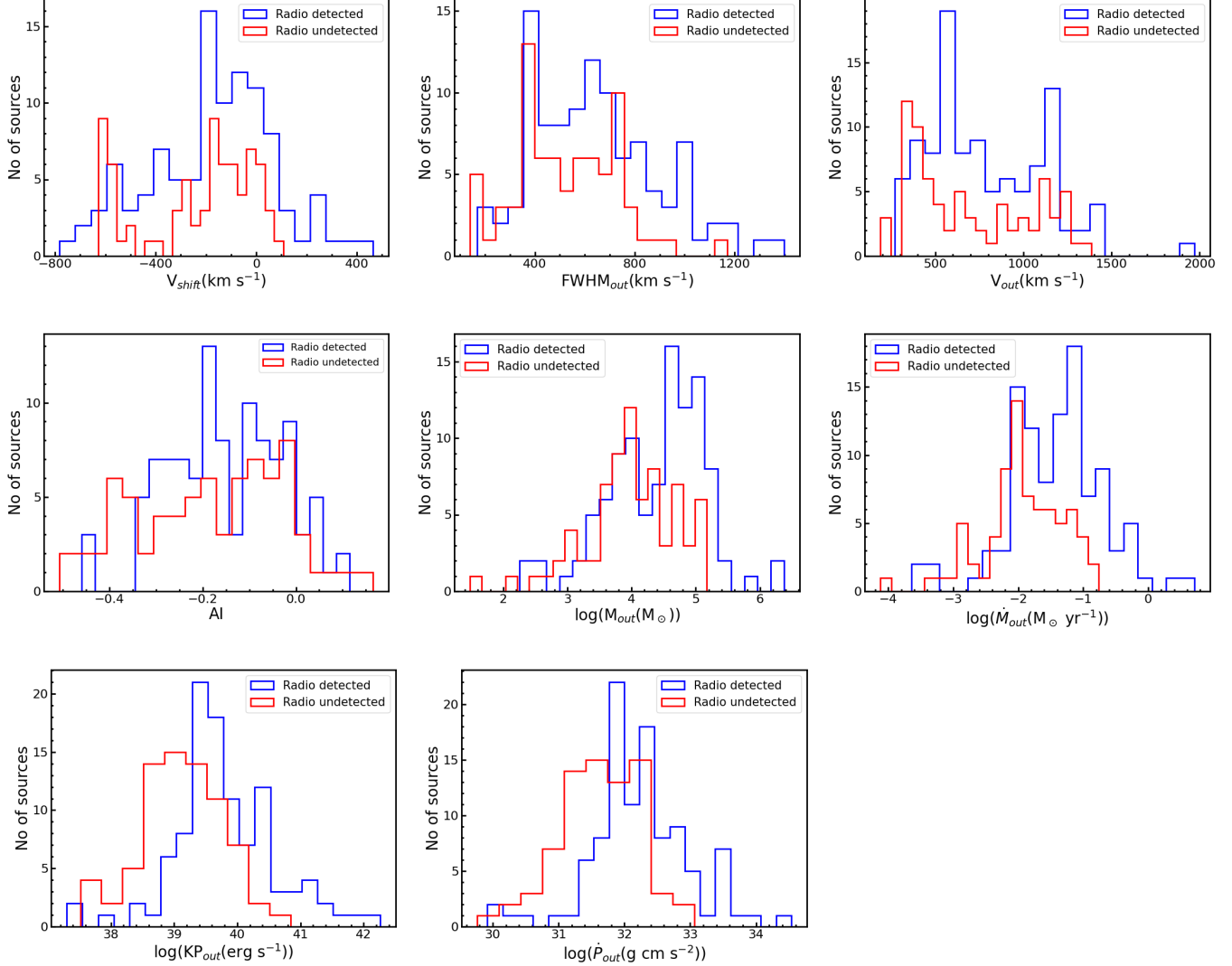


Figure 2. Histograms of different kinematics properties of outflows. The parameters are labelled in the respective plots. The blue and red histograms are for the radio-detected and radio-undetected samples, respectively.

fault, we converted them to the AB magnitude system following the guidelines provided at <https://wise2.ipac.caltech.edu/docs/release/allsky/expsup/sec4.4h.html>.

We generated a colour-colour diagram using $W2-W3$ and $W1-W2$ in the AB system for both the radio-detected and radio-undetected samples, and this is depicted in the left and middle panels of Fig. 3. Sources in this plot are classified into star formation and AGN, with a division at $W2-W3 = 0.8$. According to this division (Sabater et al. 2019), sources to the left are AGN dominated, and sources to the right are star formation dominated. Thus, in our radio-detected and radio-undetected sample, a large fraction of sources with outflows lie in the region occupied by star-forming galaxies. Recently, Salem et al. (2024) found that sources with

$W2 - W3 < 0.16$ in the AB system have very low specific star formation rate (sSFR) of $10^{-11.5} \text{ yr}^{-1}$.

We also investigated the $W3-W4$ colour, of our sample of sources with detected outflows, the distribution of which is shown in the right panel of Fig. 3 in the Vega system. Here, too, sources with $W3-W4 < 2.5$ are AGN dominated, while sources with $W3-W4 > 2.5$ are star formation dominated (Caccianiga et al. 2015). The infrared colour-colour diagram and the $W3-W4$ colour indicate that a significant portion of sources with detected outflows falls within the region typically associated with star-forming galaxies, despite all our sources being classified as AGN based on the BPT diagram. This suggests that infrared colour is not a reliable metric for distinguishing between AGN-dominated and star-formation dominated sources.

Table 2. Kinematic properties of the brightest outflows of Radio-detected sources (upper panel) and Radio-undetected sources (lower panel)

Parameter	Total			Seyferts			LINERs		
	Range	Mean	Median	Range	Mean	Median	Range	Mean	Median
$V_{shift}(\text{km s}^{-1})$	−782 to 463	−178	−163	−782 to 463	−106	−89	−695 to 258	−376	−449
$\text{FWHM}_{out}(\text{km s}^{-1})$	169 to 1398	646	626	169 to 1398	635	611	257 to 1018	678	737
$V_{out}(\text{km s}^{-1})$	271 to 1970	788	705	271 to 1970	720	642	378 to 1400	973	1084.0
AI	−0.46 to 0.12	−0.15	−0.16	−0.34 to 0.12	−0.14	−0.15	−0.46 to 0.11	−0.18	−0.16
$M_{out}(10^2 \text{ M}_\odot)$	1.81 to 23681.85	1069.71	348.47	1.89 to 23681.85	1362.98	507.71	1.81 to 2120.98	273.70	41.16
$\dot{M}_{out}(10^{-3} \text{ M}_\odot \text{ yr}^{-1})$	0.23 to 5112.32	166.56	43.28	0.23 to 5112.32	212.13	59.45	0.33 to 424.39	42.87	8.02
$\text{KP}_{out}(10^{38} \text{ erg s}^{-1})$	0.20 to 18166.25	461.92	48.25	0.24 to 18166.25	591.12	55.63	0.20 to 1425.12	111.26	34.40
$\dot{P}_{out}(10^{30} \text{ g cm s}^{-2})$	0.83 to 34222.09	923.43	165.39	0.83 to 34222.09	1177.20	198.87	0.91 to 2761.69	234.64	60.19

Parameter	Total			Seyferts			LINERs		
	Range	Mean	Median	Range	Mean	Median	Range	Mean	Median
$V_{shift}(\text{km s}^{-1})$	−628 to 108	−234	−167	−628 to 108	−173	−134	−624 to −211	−526	−585
$\text{FWHM}_{out}(\text{km s}^{-1})$	140 to 1171	526	518	140 to 865	485	443	580 to 1171	720	672
$V_{out}(\text{km s}^{-1})$	118 to 1387	691	610	188 to 1274	598	487	849 to 1387	1137	1136
AI	−0.51 to 0.16	−0.18	−0.17	−0.51 to 0.16	−0.15	−0.13	−0.44 to −0.01	−0.33	−0.37
$M_{out}(10^2 \text{ M}_\odot)$	0.30 to 1488.24	252.60	96.10	4.70 to 1488.25	288.80	114.74	0.30 to 616.59	79.95	33.35
$\dot{M}_{out}(10^{-3} \text{ M}_\odot \text{ yr}^{-1})$	0.080 to 173.53	26.34	11.34	0.95 to 173.53	27.85	12.61	0.08 to 151.93	19.11	7.42
$\text{KP}_{out}(10^{38} \text{ erg s}^{-1})$	0.33 to 696.00	42.20	12.92	0.33 to 296.34	33.46	12.88	0.36 to 696.00	83.90	22.41
$\dot{P}_{out}(10^{30} \text{ g cm s}^{-2})$	0.58 to 1154.74	106.05	50.95	1.99 to 793.52	98.54	49.45	0.58 to 1154.74	141.85	50.95

Our analysis indicates that sources exhibiting outflows tend to have redder infrared (IR) colours, as illustrated in Fig. 3. Additionally, we find a positive correlation between the IR colours W1–W2 and W3–W4 and the luminosity of the outflowing component (Fig. 4) in both cases. Interestingly, the correlation is stronger for the W3–W4 colour compared to W1–W2. This pattern is consistent across both the radio-detected and radio-undetected samples. These correlations suggest that dust in the vicinity of the outflows is likely the dominant contributor to the observed mid-infrared (MIR) emission.

Furthermore, the AGN in our sample, classified based on their BPT diagnostics, display increased redness in outflowing sources (see Fig. 3 and Fig. 4), which can be attributed to polar dust scattering. Dust grains absorb ultraviolet (UV) and optical radiation, re-emitting it in the IR and thus producing the observed redder colours. This process not only affects the IR emission but also alters the ionization conditions of the surrounding gas, potentially influencing the chemical composition of the outflows and aiding the formation of various molecules (Järvälä et al. 2022).

Our results are in agreement with Zhang et al. (2013) who found that the MIR covering factor (the ratio of MIR luminosity to bolometric luminosity) correlates with the outflow component of [OIII] λ 5007, with the correlation strengthening at longer wavelengths. This

was interpreted as evidence for IR emission produced by dust embedded within the outflows. Observations of several Seyfert galaxies also reveal that a significant fraction of their MIR emission originates along their polar directions, extending from a few parsecs to several hundred parsecs from the central engine. This emission is likely due to dust in the narrow-line region and/or dust driven by outflows (Hönig et al. 2013; Stalevski et al. 2019; Haidar et al. 2024).

4.5. Contribution of star formation to the outflows

In the previous section, it was observed that the infrared properties of outflows reveal a redder colour similar to that of star-forming galaxies. This raises the need to assess the contribution of star formation to the outflows in our sample of sources, where outflows were detected. Though the sources are classified as AGN according to the BPT diagrams, the influence of nuclear star formation could still be present in them. We aimed to assess the role of star formation in influencing outflows in the central 500×500 square pc region, which necessitates investigation of the star formation characteristics. Numerous well-established tracers of star formation exist, such as strong emission lines in optical and infrared bands, as well as continuum emission from UV to radio wavelengths (Kennicutt & Evans 2012). However, these tracers are often contaminated by AGN emissions. Recently, Spindler et al. (2018) demonstrated

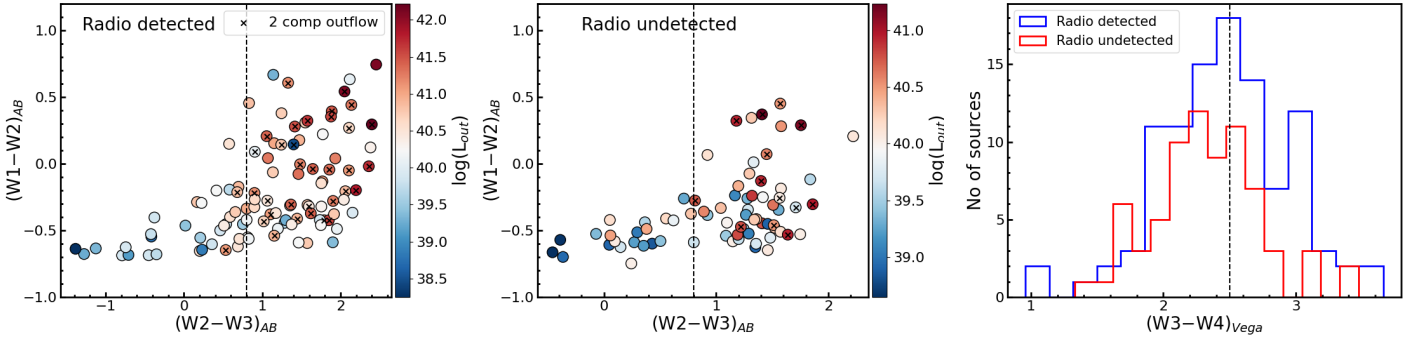


Figure 3. Infrared colour-colour diagram for the sources with outflows in the radio-detected sample (left panel) and radio-undetected sample (middle panel). Black crosses refer to sources with two outflow components. The colour bar on the right indicates the total luminosity of the outflowing gas, and the vertical dashed line is the dividing line between AGN (left) and star-forming (right) according to Sabater et al. (2019). The right panel shows the distribution of W3–W4 colour. Here too, the vertical line at W3–W4 in 2.5 is the dividing line between AGN (left of the line) and star-forming (right of the line) sources (Caccianiga et al. 2015).

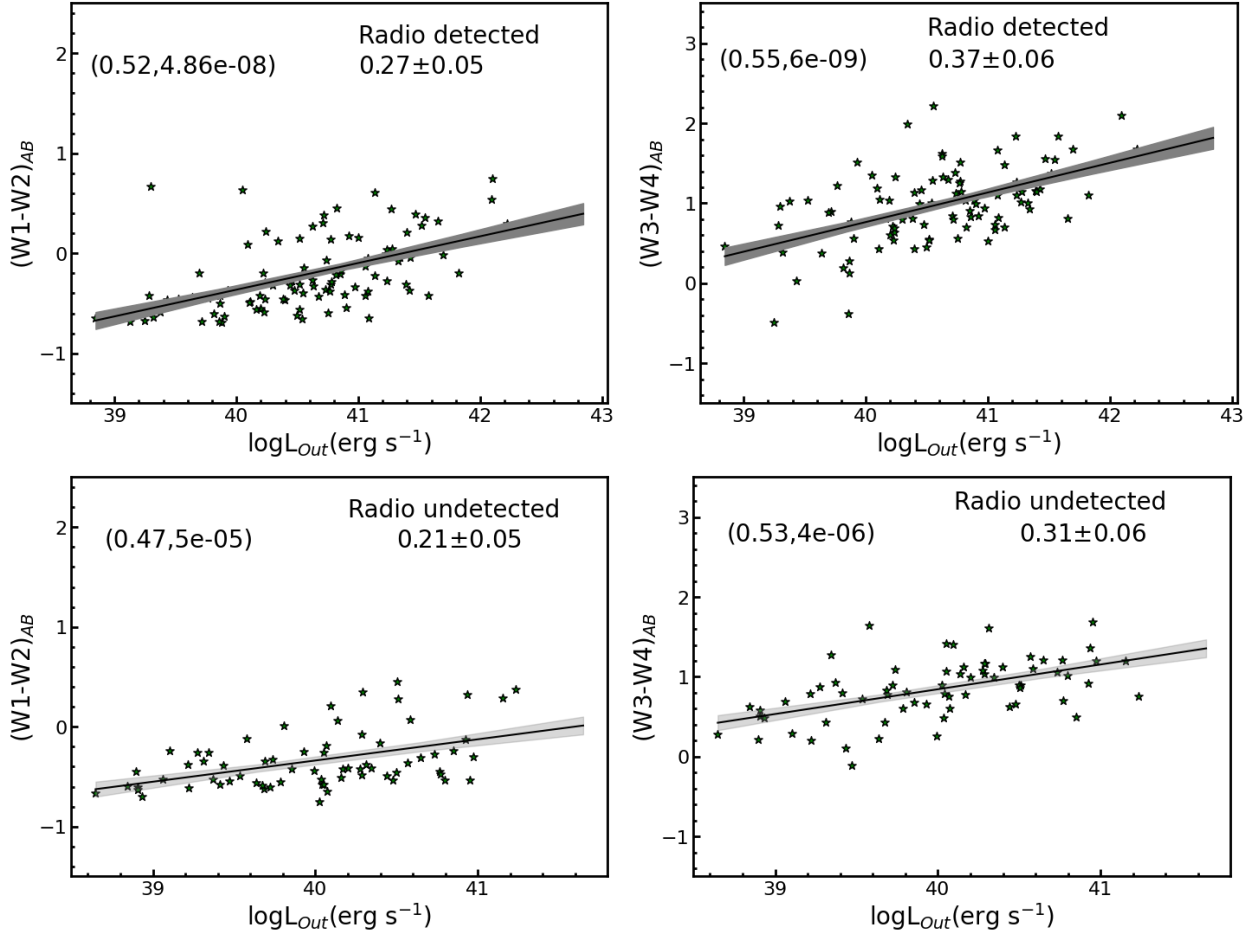


Figure 4. Variation of infrared colours with outflow luminosity for radio-detected sample (upper panel) and for radio-undetected sample (lower panel). The correlation coefficient and p-value from the KS test are displayed in the upper-left corner of each plot, while the slope (see Section 4.8) is indicated in the upper-right corner.

that the sSFR derived from the Balmer 4000 Å break strength (D_n4000) is less impacted by AGN emission lines and thus can be a better diagnostic to constrain star formation (Wilkins et al. 2024). Consequently, we employed this method to examine the sSFR in our sample of sources.

We calculated D_n4000 by taking the ratio of the average of the flux density measurements in the blue spectral range (3525–3625 Å) to the average of the flux density measurements in the red spectral range (4150–4250 Å). This is defined as

$$D_n4000 = \frac{\int_{4150}^{4250} f_\lambda d\lambda / \int_{4150}^{4250} d\lambda}{\int_{3525}^{3625} f_\lambda d\lambda / \int_{3525}^{3625} d\lambda} \quad (5)$$

The chosen spectral window is slightly different from the one originally defined by Bruzual A. (1983), however, captures the break cleanly and does not cover the metal absorption lines (see also Wilkins et al. 2024 for the use of alternate wavelength windows). This wavelength window covers both the Balmer limit of 3645 Å which is sensitive to young galaxies and the 4000 Å break. The lower bound of the blue region for the break is determined by taking into account the instrument’s shortest wavelength coverage that corresponds to the redshifted wavelengths of all observed sources.

The value of D_n4000 parameter for our sample of radio-detected and radio-undetected sources ranges from 0.8 to 2.8. D_n4000 is close to unity for the galaxies dominated by O and B-type stars (Wilkins et al. 2024), whereas D_n4000 higher than 1.51 is for an old stellar population with age more than 1.1 Gyr (Paulino-Afonso et al. 2020).

A recent study by Bluck et al. (2020) on MaNGA sources found that regions of galaxies with D_n4000 larger than 1.45 are quenched with very low star formation, though the exact values of sSFR are not known but are less than $10^{-11.5} \text{ yr}^{-1}$. About 94% of the sources in the radio-detected sample and 99% of sources in the radio-undetected sample have D_n4000 larger than 1.45, which suggests substantially low or no star formation in this central region in our sample of sources. This may possibly be due to the negative feedback effect from AGN activity.

4.6. Origin of outflows: AGN v/s star formation

In Sections 4.4, we observed that infrared diagnostics alone are insufficient to distinguish whether strong outflows originate from AGN activity or purely from star formation. However, in Section 4.5, using optical diagnostics such as the Balmer break, we found that in sources with outflows, the star formation is very low or negligible. By combining these two diagnostic methods

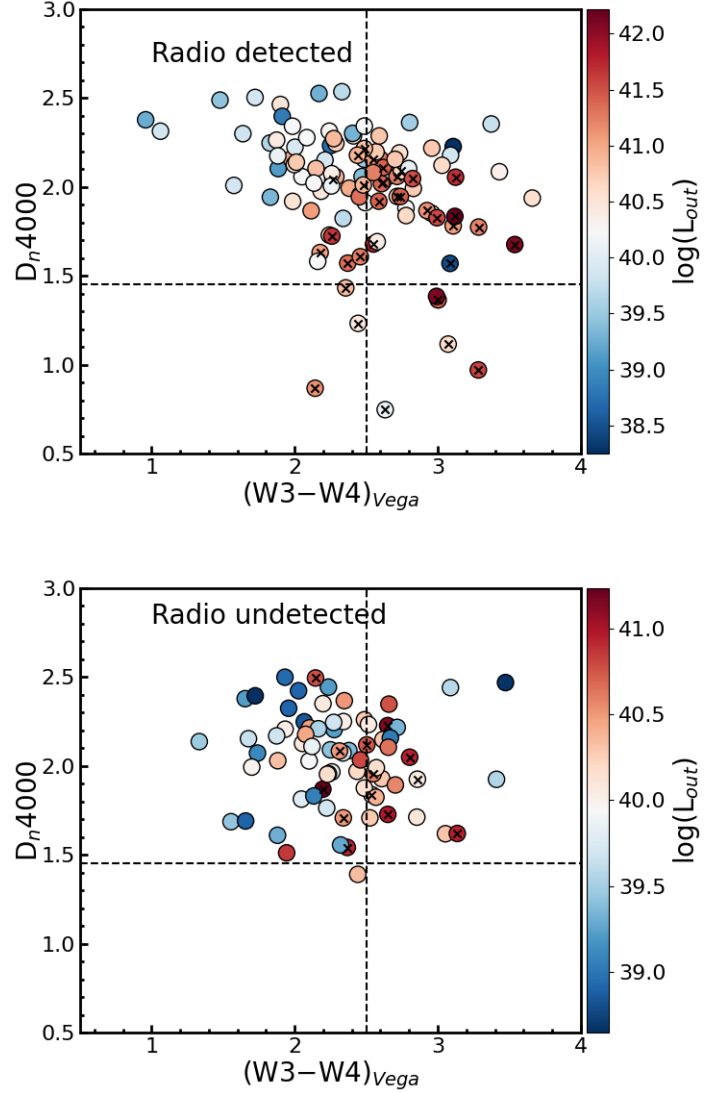


Figure 5. Position of the sources with outflows in W3–W4 vs D_n4000 plane for radio-detected (upper panel) and radio-undetected (lower panel) samples. The colour denotes the total luminosity of outflows. The black crosses are sources with two outflowing components. The vertical dashed line is $(W3 - W4)_{Vega} = 2.5$, the separation line between pure star-forming sources and AGN. The horizontal line is for $D_n4000 = 1.45$.

and analyzing the position of the sources with outflows in the D_n4000 v/s W3–W4 plane, it would be possible to identify if the detected outflows are due to star formation and/or AGN activity. We show in Fig. 5 the infrared colour versus the Balmer break plot. From this figure, it is evident that most of our sources are situated in the AGN-dominated region. This new diagnostic diagram clearly indicates that the outflows found in sources with and without radio emission are due to pro-

cesses related to AGN. About 5% of the radio-detected sources with outflows lie in the region occupied by star formation with redder colours. In all these sources, both blueshifted (approaching component of outflows) and red-shifted (receding component of outflows) were detected. The redshifted component of the outflow, being located below the plane of the galaxy, is likely to be obscured by dust, and the observations of such sources to be redder in colour is not unexpected (Belli et al. 2024). Irrespective of that, the contribution from both AGN and star formation to the observed outflows in these minority of sources could not be ruled out. Also, a large fraction of sources with $D_n4000 > 1.45$ (thus negligible star formation) have redder colours, and this is likely due to the interaction of the outflowing gas with dust (Järvellä et al. 2022).

4.7. Cause of radio emission

From Section 4.6, it is clear that the observed outflows are due to AGN in both the samples of radio-detected and radio-undetected sources. Therefore, the observed radio emission in our radio-detected sample is unlikely to be due to star formation activities in their host galaxies, however, attributed to processes related to AGN such as the presence of low power radio jets, accretion disk corona as well as shocks due to outflows (Panessa et al. 2019; Liao et al. 2024). In this section, we aim to understand the origin of radio emission in our radio-detected sample making use of diagnostic plots available in the literature. We show in Fig. 6 the location of sources with outflows in the radio-detected sample in the F_{W3} v/s $F_{1.4}$ GHz plane. For this plot, the radio flux density values were taken from the FIRST survey, while the flux density corresponding to the W3 band of WISE was taken from the WISE catalogue. Also shown in the same plot is the $F_{W3} = F_{1.4}$ line. According to Kozieł-Wierzbowska et al. (2021) sources below the line are radio AGN, while those above the line are starburst dominated AGN. We also checked the $q22$ parameter defined as

$$q22 = \log(F_{22}/F_{1.4}) \quad (6)$$

Here, F_{22} and $F_{1.4}$ are the flux densities in the W4 band of the WISE and 1.4 GHz from FIRST respectively. The histogram of the $q22$ parameter is shown in Fig. 7. Here, too, about 40% of the sources have $q22$ greater than unity, favouring star formation processes to be the cause of radio emission in them. In summary, although the $q22$ parameter and the F_{W3} v/s $F_{1.4}$ diagnostics indicate that in a large fraction of the sources, the observed radio emission is likely to be associated with star formation activity, the plot of D_n4000 against $q22$ (Fig. 7) shows that all sources barring six sources, lie in the

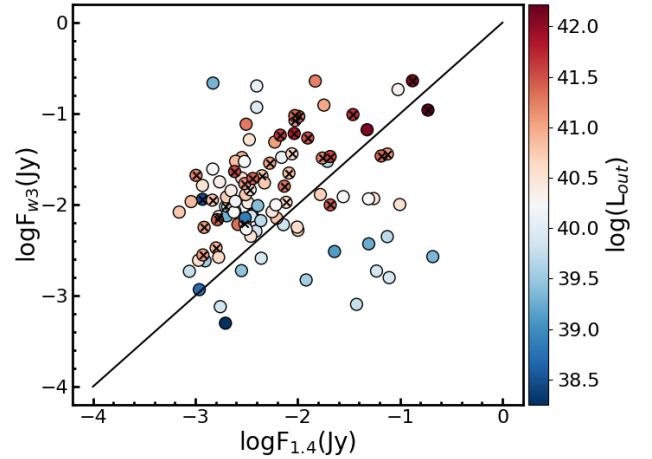


Figure 6. Location of the sources with outflows in the radio-detected sample in the $F(W3)$ v/s $F(1.4\text{GHz})$ plane. The solid black solid line is the $F_{W3} = F_{1.4}$ line. The black crosses are sources with two components of outflows. The colour denotes the luminosity of outflows.

AGN dominated region. This reddening could be due to dust scattering of AGN radiation. This reinforces that the observed radio emission in our radio-detected sample is indeed AGN dominated. High resolution radio observations are the only direct way to identify which among the processes related to AGN are the cause of the observed radio emission in our sample. Though the detection of core jet structure is an unambiguous evidence of jet that produces the observed radio emission, the resolution of FIRST images used in this work is insufficient. In the absence of this, in all further discussion, we assume that the observed radio emission is due to jet emission.

4.8. Correlation of outflow properties with physical properties of AGN

From various diagnostics, it is clear that the detected outflows are due to AGN. In this scenario, the driving force of outflows could be either from the radiation energy or the radio jets from AGN. To explore this, we analyzed the outflow properties alongside AGN properties such as the M_{BH} , bolometric luminosity (L_{Bol}) and Eddington ratio (λ_{Edd}) for both the radio-detected and radio-undetected samples as well as the radio jet power (P_{Jet}) for the radio-detected sample. We determined M_{BH} adopting the dynamical method, using the $M_{BH} - \sigma_*$ relation, where σ_* represents the stellar velocity dispersion. The σ_* values were obtained from the *Pipe3d* catalogue (Sánchez et al. 2022), derived through stellar synthesis population modelling within one effective radius. Following the relation provided in Baron &

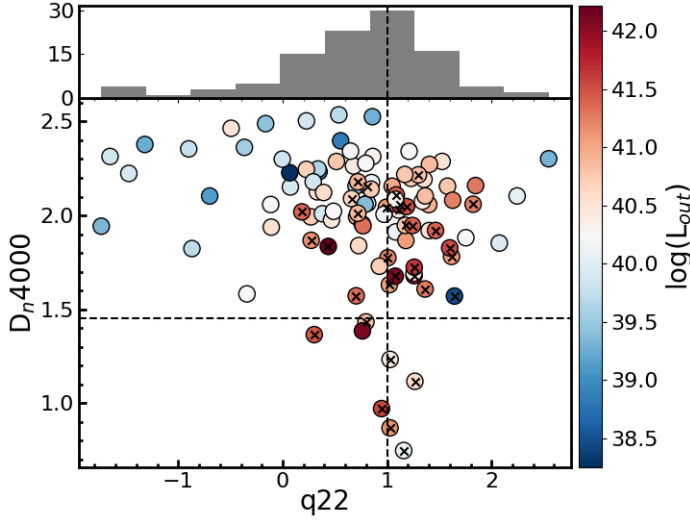


Figure 7. Position of outflow detected sources in the radio-detected sample in $q22$ vs D_n4000 plane. The vertical line is $q22 = 1.0$, and the horizontal dashed line is $D_n4000 = 1.45$.

Ménard (2019), which has been validated for both Type 1 and Type 2 AGN, by Baron & Ménard (2019), we calculated M_{BH} for all the sources in our sample.

We calculated L_{Bol} from $H\alpha$ luminosity by following Greene & Ho (2007) and Greene & Ho (2005) wherein the luminosity of the $H\alpha$ line was determined from the $H\alpha$ flux taken from DAP and corrected for extinction effect. We also calculated λ_{Edd} , from Eddington luminosity L_{Edd} , the maximum luminosity emitted if the source is in hydrodynamical equilibrium and L_{Bol} , as the ratio of L_{Bol} to L_{Edd} . The L_{Edd} defined as

$$L_{Edd} = 1.26 \times 10^{38} \left(\frac{M_{BH}}{M_{\odot}} \right) \text{erg s}^{-1} \quad (7)$$

For the sample of radio-detected sources, we estimated P_{Jet} by following Cavagnolo et al. (2010) and considering that the radio emission in these sources is jet emission. For this, we used the 1.4 GHz luminosity ($L_{1.4}$) calculated using the integrated flux densities from FIRST survey and corrected for redshift effect assuming a spectral index ($S_{\nu} \propto \nu^{-\alpha}$) of 0.7 (Condon et al. 2002). The distribution of $L_{1.4}$ for our sample of radio-detected and radio-undetected sources is shown in Fig. 8. For radio-undetected sources, the $L_{1.4}$ values are the upper limits that were calculated using the detection limit of the FIRST survey, which is 0.5 mJy.

After calculating these physical parameters of AGN, we compared them with outflow properties to explore potential correlations. In cases where two outflowing components were detected, for the total outflow rate or the total kinetic power of outflows, we used the sum of

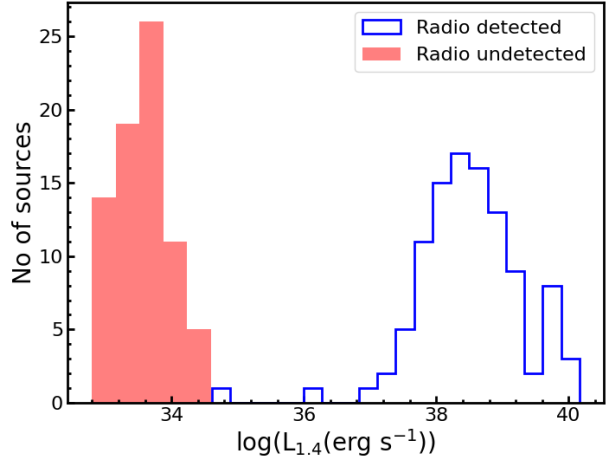


Figure 8. Distribution of $L_{1.4}$ for the radio detected sample (blue color). The shaded red region shows the upper limit of $L_{1.4}$ for the radio-undetected by considering the detection limit of the FIRST survey, which is 0.5 mJy.

the quantities deduced from both components. We performed a statistical linear correlation test, the Pearson test, to identify significant correlations in terms of correlation coefficients and p-values. For parameters exhibiting significant correlations, we employed the Bayesian linear regression method using the *LINMIX.ERR* (Kelly 2007) to fit a power-law relationship between the variables in log-log space. This method takes account of errors in both axes. If the AGN parameter is X_{AGN} and outflow parameter is Y_{out} then the fitted function has the form

$$Y_{out} = A(X_{AGN})^{\alpha} \quad (8)$$

or

$$\log(Y_{out}) = \log A + \alpha \log(X_{AGN}) \quad (9)$$

where A is the multiplication constant and α is the power-law exponent. The best-fit values for α and the correlation coefficients for different parameters are summarized in Table 3.

From Table 3, it is evident that both \dot{M}_{out} and KP_{out} are significantly correlated with L_{Bol} for both radio-detected and radio-undetected sources. This finding aligns with previous studies in the literature (Fiore et al. 2017; Bischetti et al. 2019; Musiimenta et al. 2023). While our results confirm the correlation between \dot{M}_{out} and L_{Bol} noted in earlier works, we also emphasize the differences in the correlations between the two samples. Notably, the higher correlation coefficient and lower p-values for radio-detected sources suggest that this correlation is stronger in radio-detected sources than in their radio-undetected counterparts.

Table 3. Results of the fits to the observed data. Here, R and p are the correlation coefficient and probability for no correlation, respectively for the Pearson correlation test. The quoted values of α , the power law exponent are the mean and the one standard deviation (1σ).

Parameter	Radio-detected		Radio-undetected	
$Y_{out} \text{ v/s } X_{AGN}$	(R,p)	α	(R,p)	α
$KP_{out} \text{ v/s } L_{Bol}$	(0.72, 7×10^{-18})	1.18 ± 0.14	(0.52, 2×10^{-6})	0.81 ± 0.20
$\dot{M}_{out} \text{ v/s } L_{Bol}$	(0.74, 3×10^{-19})	1.07 ± 0.12	(0.60, 9×10^{-9})	0.97 ± 0.17
$KP_{out} \text{ v/s } P_{Jet}$	(0.36, 2×10^{-4})	0.56 ± 0.14	—	—
$\dot{M}_{out} \text{ v/s } P_{Jet}$	(0.28, 0.004)	0.43 ± 0.12	—	—
$KP_{out} \text{ v/s } P_{Jet} [\log(\frac{L_{Bol}}{P_{Jet}}) > 0.4]$	(0.64, 1×10^{-11})	0.99 ± 0.14	—	—
$\dot{M}_{out} \text{ v/s } P_{Jet} [\log(\frac{L_{Bol}}{P_{Jet}}) > 0.4]$	(0.58, 5×10^{-9})	0.79 ± 0.12	—	—

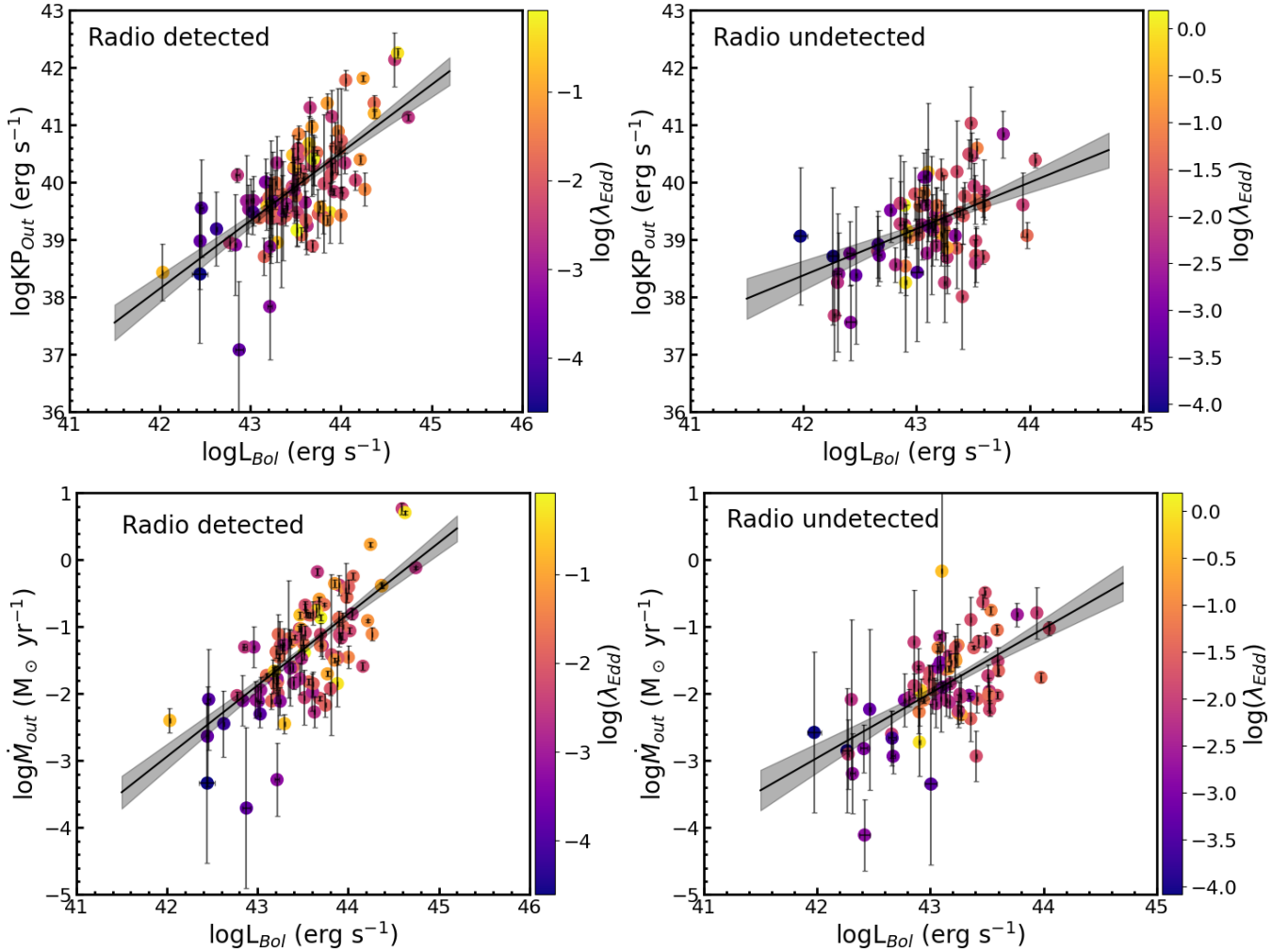


Figure 9. Upper panel: Variation of total kinetic power of warm ionized outflow with L_{Bol} for radio-detected (left panel) and radio-undetected sources (right panel). Lower panel: Variation of total outflow rate with L_{Bol} for the radio-detected sources (left panel) and radio-undetected sources (right panel). In each plot, the scatter points represent our data with 1σ error bars, while the solid line and shaded region indicate the fitted line with a 1σ confidence band. The color in each plot corresponds to λ_{Edd} .

Examining the relationship of these outflow parameters with AGN luminosity, we found that for the radio-detected sample, we observed $\dot{M}_{out} \propto L_{Bol}^{1.07 \pm 0.12}$. In contrast, for the radio-undetected sample, $\dot{M}_{out} \propto L_{Bol}^{0.97 \pm 0.17}$. Though the slopes are consistent within 1σ , KP_{out} demonstrates a more pronounced difference: we found $KP_{out} \propto L_{Bol}^{1.18 \pm 0.14}$ for radio-detected sources, while for the radio-undetected sample, we found $KP_{out} \propto L_{Bol}^{0.81 \pm 0.20}$. This indicates a steeper slope by 1σ for the radio-detected sources compared to their undetected counterparts. This trend is illustrated in Fig. 9, where we plot L_{Bol} against KP_{out} and \dot{M}_{out} , color-coded by λ_{Edd} . In the radio-detected category of sources, those with larger λ_{Edd} preferentially occupy the region with larger KP_{out} . This suggests a relationship between outflow power and λ_{Edd} for these sources. Conversely, this trend is not as clear for radio-undetected sources, as depicted on the right side of Fig. 9.

The correlations observed in Fig. 9, suggest multiple mechanisms are at play in driving outflows for radio-detected sources. While radiation from AGN is likely the primary driver of outflows in both radio-detected and radio-undetected sources, radio jets may serve as an additional mechanism that enhances outflow kinematics in radio-detected sources. This could explain the steeper correlation between KP_{out} and L_{Bol} in the radio-detected sample and the stronger correlation of KP_{out} with λ_{Edd} . Although there is a general upward trend of outflow properties with L_{Bol} , the scatter in the plots (see Fig. 9) may be attributed to the complex interplay between outflows and the quantity or geometry of dense gas in the nuclear regions of these sources (Ramos Almeida et al. 2022). Moreover, the colour coding in Fig. 9 indicates that sources with high λ_{Edd} tend to have elevated values of L_{Bol} , \dot{M}_{out} , and KP_{out} . This interpretation highlights the nuanced role of AGN radiation and radio jets in influencing outflow characteristics, suggesting a more complex feedback mechanism that merits further investigation.

For the radio-detected sample of sources, we found a flat relation between the outflow properties and jet power. We obtained the best fit scaling relation of $KP_{out} \propto P_{Jet}^{0.56 \pm 0.14}$ and $\dot{M}_{out} \propto P_{Jet}^{0.43 \pm 0.12}$. The results of the fits are given in Table 3. We also found the ratio of $\log(\frac{L_{Bol}}{P_{Jet}})$ to have a bimodal behaviour with a dividing limit at 0.4. We noticed beyond this limit, P_{Jet} is very strongly correlated with L_{Bol} with a slope of 0.96 ± 0.06 which can be seen in the upper panel of Fig. 10. In the lower panel of Fig. 10, we show the correlation between KP_{out} and P_{Jet} . Here, the sources are colour coded with $\log(\frac{L_{Bol}}{P_{Jet}})$. We found that beyond the limit of $\log(\frac{L_{Bol}}{P_{Jet}})=0.4$ i.e. for $\log(\frac{L_{Bol}}{P_{Jet}})>0.4$ the cor-

relation between KP_{out} and P_{Jet} is significantly strong and steep with $KP_{out} \propto P_{Jet}^{0.99 \pm 0.14}$. Below this limit, i.e. for higher P_{Jet} with similar L_{Bol} , KP_{out} is lower. This may be due to high power jet encountering lower interaction with the cloud where [OIII] $\lambda 5007$ originates, reducing the outflow luminosity and leading to low outflow characteristics such as KP_{out} and \dot{M}_{out} . Alternatively, a high-power jet can ionize the gas to its higher ionization state, leading to low luminous outflow. Thus at any jet power, significant dominance of the jet power over bolometric luminosity can lead to weaker outflows.

This interpretation highlights the nuanced role of AGN radiation and radio jets in shaping outflow characteristics, suggesting a more complex feedback mechanism that warrants deeper exploration. Future studies can leverage high-resolution, multi-wavelength observations to clarify the relative contributions of radiation-driven and jet-driven feedback processes. Spatially resolved spectroscopic studies, combined with detailed radio imaging, can help establish a clearer link between jet morphology and outflow kinematics. Additionally, theoretical modelling and simulations can provide further insights into the interplay between AGN-driven winds, jets, and the surrounding ISM. Investigating these aspects across a broader range of AGN types and host environments will be crucial for building a more comprehensive understanding of AGN feedback and its impact on galaxy evolution.

5. SUMMARY

In this study, we conducted a comparative analysis of outflow properties in radio-detected and radio-undetected sources in their central region of 500×500 square pc. Our total sample consists of 538 AGN with detected [OIII] $\lambda 5007$ line, mainly Seyfert and LINER type, of which 197 are radio-detected and 341 are radio-undetected. The objective was to identify outflows, study their properties, and constrain the role of AGN radiation and/or jets in driving outflows. For this, we used spatially resolved optical spectroscopic data from MaNGA and radio observations from FIRST surveys. We studied the properties of outflows and then compared them with AGN properties. Additionally, we explored the relationship between radio properties and outflow characteristics within the radio-detected sources. We summarize our main findings below.

1. To detect outflows, we carried out multiple Gaussian fits to the observed [OIII] $\lambda 5007$ line. In the radio-detected sample, $56 \pm 7\%$ of sources showed evidence of outflows. However, in the radio-undetected sample, $25 \pm 3\%$ of sources showed outflows. Thus, in our sample, the outflow detection

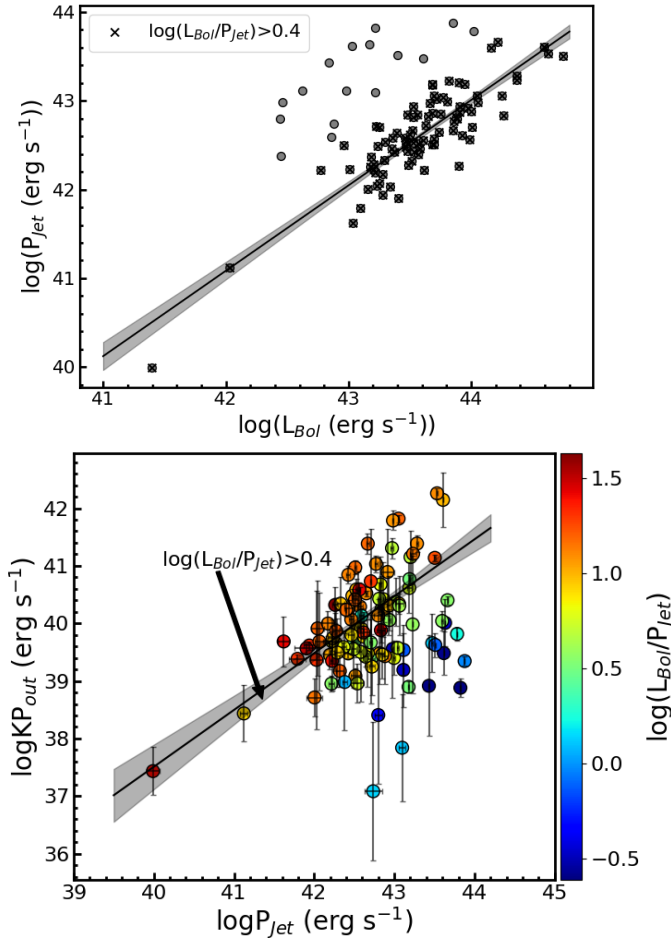


Figure 10. Upper panel: Jet power vs bolometric luminosity. The sources with $\log(\frac{L_{Bol}}{P_{jet}}) > 0.4$ are shown with crosses. The fitted line is for the sources with $\log(\frac{L_{Bol}}{P_{jet}}) > 0.4$. Lower panel: The variation of kinetic power of outflow with jet power. The solid line with the shaded region is the fitted line with 1 σ uncertainty for the given condition. The colour in each plot corresponds to $\frac{L_{Bol}}{P_{jet}}$ in the log scale.

rate is higher in radio-detected sources compared to radio-undetected sources.

2. On separating our sample of sources into Seyferts and LINERs, outflows are detected more in Seyferts ($66 \pm 7\%$) relative to LINERs ($15 \pm 2\%$). This is true for both the radio-detected and radio-undetected samples. The mass outflow rate and outflow power are higher for Seyferts than LINERs, but the velocity structures are higher for LINERs compared to Seyferts.
3. In both the radio-detected and radio-undetected sample, for a majority of sources ($\sim 80\%$), we found the [OIII] $\lambda 5007$ line to have a blue asymme-

try in addition to the narrow component. Also, in a minority of sources, in addition to the blueshifted component, we also observed the redshifted component. The blueshifted component could be the approaching side of the outflow located above the plane of the galaxy, and the redshifted component could be the receding side of the outflow, located below the plane of the galaxy.

4. We observed distinct differences in the kinematics of the outflowing gas between the radio-detected and radio-undetected samples. The radio-detected sources exhibit higher velocity, larger velocity dispersion, greater asymmetry, larger outflow mass, and stronger kinematic power compared to the radio-undetected sources.
5. We found that in the infrared bands, more luminous outflows appear redder in colour compared to weaker outflows. Infrared colours show a positive correlation with outflow luminosity, with this dependence becoming more pronounced in the mid-infrared band. This trend is primarily attributed to the presence of larger amounts of polar dust in the more powerful outflows.
6. We found a strong correlation between the outflow characteristics, such as the \dot{M}_{out} and KP_{out} of the outflow with the L_{Bol} . Such a correlation points to radiation from AGN being the primary driver for outflows in both radio-detected and radio-undetected samples. However, this correlation between the outflow characteristics with the bolometric luminosity is mildly steeper for the radio-detected sample compared to the radio-undetected sample. This suggests that in the radio-detected sample, radio jets could play an additional modest secondary role over and above the dominant role played by radiation in enhancing outflow kinematics.
7. Outflow characteristics are also found to show a correlation with λ_{Edd} . Sources with higher λ_{Edd} appear to have higher L_{Bol} , \dot{M}_{out} and KP_{out} . This is true for both the radio-detected and radio-undetected samples.
8. For the radio-detected sample, we observed a bimodality in the distribution of $\log(\frac{L_{Bol}}{P_{jet}})$, with the dividing line at $\log(\frac{L_{Bol}}{P_{jet}}) = 0.4$. In the correlation between the kinetic power of outflows and jet power, we found that at any jet power, significant dominance of the jet power over the bolometric luminosity can lead to weaker outflows.

9. We found the value of the D_n4000 parameter for our sample of radio-detected and radio-undetected sources to range between 0.8 and 2.8. About 94% of the sources in the radio-detected sample and 99% of sources in the radio-undetected sample have D_n4000 larger than 1.45, pointing to sSFR lesser than $10^{-11.5} \text{ yr}^{-1}$, which may possibly be due to negative AGN feedback.

Our findings suggest that ionized gas outflows, driven by the interaction between AGN radiation/winds and the ISM, are common across all AGN. However, the presence of radio jets appears to affect gas kinematics further, leading to a higher rate of outflow detection in radio-detected sources, as evidenced by our study. Further investigations using high-resolution, multi-wavelength observations for different types of AGN may provide more insights towards understanding the feedback processes of radiation/winds and jets in greater detail. For example, high-resolution radio observations along with observations at other wavelengths would allow for a detailed spatial correlation between the morphology of radio jets and the outflowing gas, and understanding their kinematics.

6. ACKNOWLEDGMENTS

We thank the reviewer for their comments and suggestions, which have helped to improve the manuscript. We also acknowledge Dr. Chris Harrison, at Newcastle University for useful suggestions in the initial stage. This publication uses data from the MaNGA (Mapping Nearby Galaxies at APO) survey, which is one of the Sloan Digital Sky Survey (SDSS) IV programs. Funding for the Sloan Digital Sky Survey IV has been provided by the Alfred P. Sloan Foundation, the U.S. Department of Energy Office of Science, and the Participating Institutions.

SDSS-IV acknowledges support and resources from the Center for High Performance Computing at the University of Utah. The SDSS website is www.sdss4.org.

SDSS-IV is managed by the Astrophysical Research Consortium for the Participating Institutions of the SDSS Collaboration including the Brazilian Participation Group, the Carnegie Institution for Science, Carnegie Mellon University, Center for Astrophysics — Harvard & Smithsonian, the Chilean Participation Group, the French Participation Group, Instituto de Astrofísica de Canarias, The Johns Hopkins University, Kavli Institute for the Physics and Mathematics of the Universe (IPMU) / University of Tokyo, the Korean Participation Group, Lawrence Berkeley National Laboratory, Leibniz Institut für Astrophysik Potsdam (AIP), Max-Planck-Institut für Astronomie (MPIA Heidelberg), Max-Planck-Institut für Astrophysik (MPA Garching), Max-Planck-Institut für Extraterrestrische Physik (MPE), National Astronomical Observatories of China, New Mexico State University, New York University, University of Notre Dame, Observatório Nacional / MCTI, The Ohio State University, Pennsylvania State University, Shanghai Astronomical Observatory, United Kingdom Participation Group, Universidad Nacional Autónoma de México, University of Arizona, University of Colorado Boulder, University of Oxford, University of Portsmouth, University of Utah, University of Virginia, University of Washington, University of Wisconsin, Vanderbilt University, and Yale University. This project makes use of the MaNGA-Pipe3D dataproducts. We thank the IA-UNAM MaNGA team for creating this catalogue, and the Conacyt Project CB-285080 for supporting them.

This publication uses radio observations carried out using the National Radio Astronomy Observatory facilities Very Large Array (VLA) of FIRST survey. The National Radio Astronomy Observatory is a facility of the National Science Foundation operated under a cooperative agreement by Associated Universities, Inc. This work has made use of the NASA Astrophysics Data System (ADS)³ and the NASA/IPAC extragalactic database (NED)⁴. PN thanks the Council of Scientific and Industrial Research (CSIR), Government of India, for supporting her research under the CSIR Junior/Senior research fellowship program through the grant no. 09/079(2867)/2021 – *EMR – I*.

Facilities: SDSS, MaNGA, FIRST

Software: Topcat (Taylor 2005), Numpy (Harris et al. 2020), Astropy (Astropy Collaboration et al. 2022),

Scipy (Virtanen et al. 2020), Matplotlib (Hunter 2007), PyNeb (Luridiana et al. 2015), LINMIX_ERR (Kelly 2007)

APPENDIX

A. SAMPLE AND EMISSION LINE FITS

As described in Section 2, our sample to study the mechanisms that trigger warm ionised outflows in AGN, is from MaNGA, which contains both AGN and non-AGN sources. We, therefore selected the AGN sources by constructing BPT diagrams. The positions of the sources in the final sample in the BPT diagrams are shown in Fig. A1. The AGN sources thus selected were divided into radio-detected and radio-undetected ones.

The distribution of the sources in the redshift and optical B-band brightness plane is shown in Fig. A2.

To identify warm ionised outflows in the final sample of AGN, we carried out Gaussian fits to the [OIII] λ 5007 line. Sample fits are shown in Fig. A3.

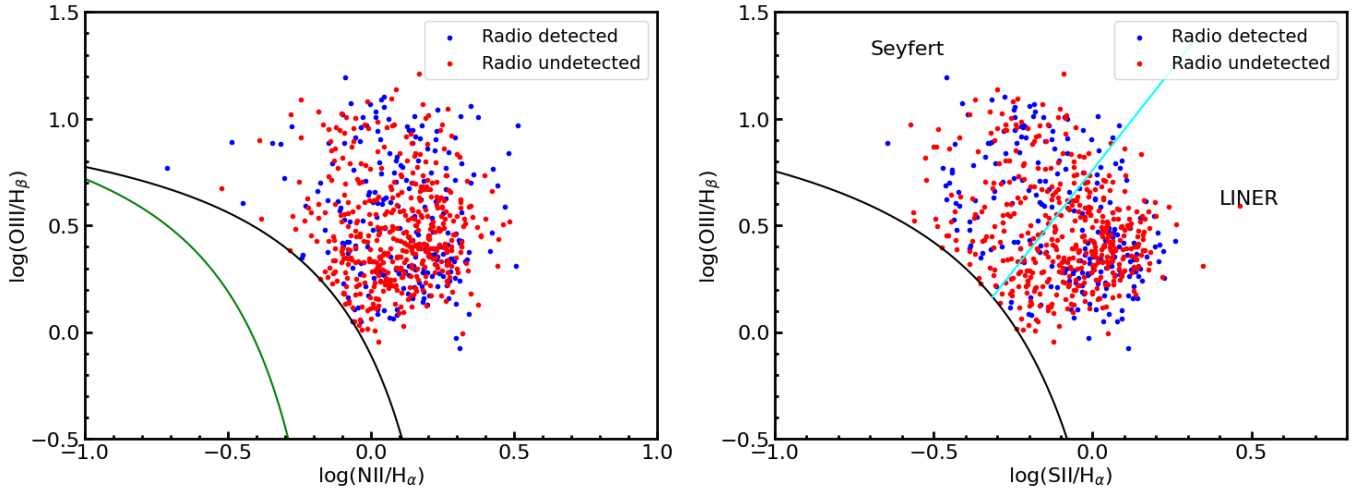


Figure A1. Positions of the sources in the [NII]/H α BPT diagram (left) and [SII]/H α BPT diagram (right). The black and green solid lines separate the region occupied by AGN and star-forming galaxies according to Kewley et al. (2001) and Kauffmann et al. (2003), respectively. The cyan solid line separates Seyfert galaxies and LINERs (Kewley et al. 2001). Filled blue and red circles refer to radio-detected and radio-undetected sources.

B. KINEMATICS PROPERTIES OF THE LESS LUMINOUS AND HIGH-SPEED OUTFLOWS

To investigate the kinematic properties of the outflows in both the radio-detected and radio-undetected samples (Section 4.2), we have initially used the brightest components, the results for which are given in Table 2. We also carried out a similar analysis using the less-luminous outflows and the higher velocity outflows, the results of which are given in Tables B1 and B2 respectively.

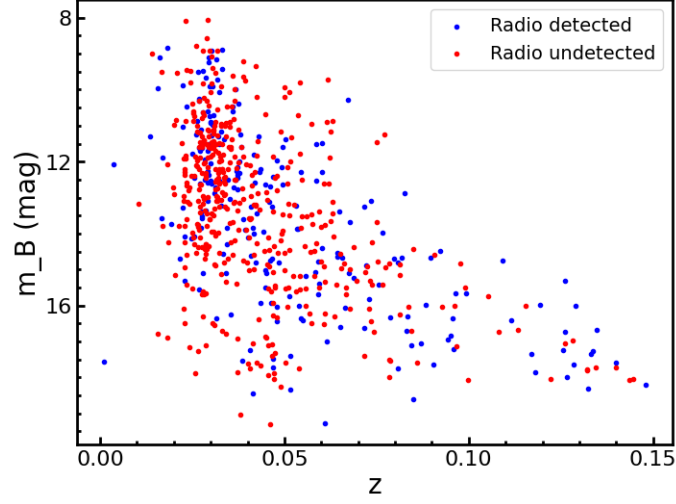


Figure A2. Distribution of sources in the redshift z /s B-band apparent magnitude plane. Here, the filled blue and red circles refer to the radio-detected and radio-undetected sources, respectively.

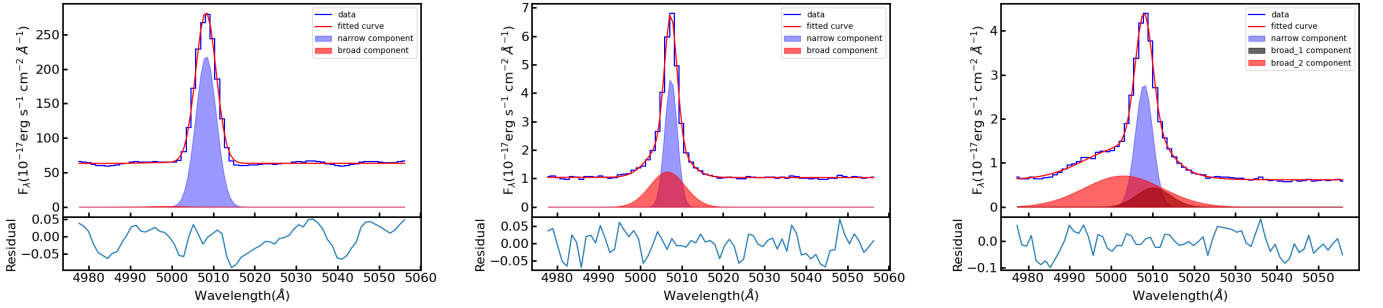


Figure A3. Example line fits to the [OIII] λ 5007 line for an outflow undetected (left panel) and an outflow detected (middle and right panels) source. A single Gaussian profile nicely describes the observed line profile (left panel), while two and three Gaussian components (two phases of outflow) were required for the observed line profiles in the middle and right panels. The broad Gaussian components in the middle and right panels show the presence of outflow.

Table B1. Kinematic properties of the less luminous outflows of Radio-detected sources (upper panel) and Radio-undetected sources (lower panel)

Parameter	Total			Seyferts			LINERs		
	Range	Mean	Median	Range	Mean	Median	Range	Mean	Median
$V_{shift}(\text{km s}^{-1})$	−695.0 to 882.0	−194.0	−198.0	−583.0 to 882.0	−127.0	−163.0	−695.0 to 258.0	−376.0	−449.0
$\text{FWHM}_{out}(\text{km s}^{-1})$	156.0 to 1401.0	653.0	635.0	156.0 to 1401.0	644.0	619.0	257.0 to 1018.0	678.0	737.0
$V_{out}(\text{km s}^{-1})$	308.0 to 1503.0	823.0	818.0	308.0 to 1503.0	768.0	733.0	378.0 to 1400.0	973.0	1084.0
AI	−0.46 to 0.12	−0.15	−0.16	−0.34 to 0.12	−0.14	−0.15	−0.46 to 0.11	−0.18	−0.16
$M_{out}(10^2 M_{\odot})$	1.11 to 23558.28	775.31	235.03	1.11 to 23558.28	960.12	348.17	1.81 to 2120.98	273.7	41.16
$\dot{M}_{out}(10^{-3} M_{\odot} \text{ yr}^{-1})$	0.07 to 5112.32	145.64	33.95	0.07 to 5112.32	183.5	43.07	0.33 to 424.39	42.87	8.02
$\text{KP}_{out}(10^{38} \text{ erg s}^{-1})$	0.02 to 18166.25	489.61	47.73	0.02 to 18166.25	629.0	62.1	0.2 to 697.58	124.27	57.6
$\dot{P}_{out}(10^{30} \text{ g cm s}^{-2})$	0.14 to 34222.09	922.0	134.0	0.14 to 34222.09	1175.24	181.62	0.91 to 2761.69	234.64	60.19

Parameter	Total			Seyferts			LINERs		
	Range	Mean	Median	Range	Mean	Median	Range	Mean	Median
$V_{shift}(\text{km s}^{-1})$	−657.0 to 227.0	−277.0	−235.0	−657.0 to 227.0	−225.0	−186.0	−624.0 to −211.0	−526.0	−585.0
$\text{FWHM}_{out}(\text{km s}^{-1})$	152.0 to 1171.0	560.0	577.0	152.0 to 1151.0	527.0	505.0	580.0 to 1171.0	720.0	672.0
$V_{out}(\text{km s}^{-1})$	237.0 to 1387.0	769.0	733.0	237.0 to 1343.0	692.0	643.0	849.0 to 1387.0	1137.0	1136.0
AI	−0.51 to 0.16	−0.18	−0.17	−0.51 to 0.16	−0.15	−0.13	−0.44 to −0.01	−0.33	−0.37
$M_{out}(10^2 M_{\odot})$	0.3 to 1481.81	202.86	78.37	4.7 to 1481.81	228.63	91.57	0.3 to 616.59	79.95	33.35
$\dot{M}_{out}(10^{-3} M_{\odot} \text{ yr}^{-1})$	0.08 to 247.09	24.88	9.87	1.08 to 247.09	26.1	11.58	0.08 to 151.93	19.11	7.42
$\text{KP}_{out}(10^{38} \text{ erg s}^{-1})$	0.36 to 1053.8	59.27	14.97	0.46 to 1053.8	54.11	14.42	0.36 to 696.0	83.9	22.41
$\dot{P}_{out}(10^{30} \text{ g cm s}^{-2})$	0.58 to 1812.07	123.71	52.05	2.63 to 1812.07	119.91	55.32	0.58 to 1154.74	141.85	50.95

Table B2. Kinematic properties of the high-speed outflows of Radio-detected sources (upper panel) and Radio-undetected sources (lower panel)

Parameter	Total			Seyferts			LINERs		
	Range	Mean	Median	Range	Mean	Median	Range	Mean	Median
$V_{shift}(\text{km s}^{-1})$	−782.0 to 882.0	−198.0	−193.0	−782.0 to 882.0	−133.0	−133.0	−695.0 to 258.0	−376.0	−449.0
$\text{FWHM}_{out}(\text{km s}^{-1})$	176.0 to 1401.0	728.0	682.0	176.0 to 1401.0	731.0	679.0	257.0 to 1018.0	678.0	737.0
$V_{out}(\text{km s}^{-1})$	337.0 to 1970.0	879.0	864.0	337.0 to 1970.0	844.0	826.0	378.0 to 1400.0	973.0	1084.0
AI	−0.46 to 0.12	−0.15	−0.16	−0.34 to 0.12	−0.14	−0.15	−0.46 to 0.11	−0.18	−0.16
$M_{out}(10^2 M_{\odot})$	1.81 to 23558.28	831.92	239.35	1.89 to 23558.28	1037.58	384.92	1.81 to 2120.98	273.7	41.16
$\dot{M}_{out}(10^{-3} M_{\odot} \text{ yr}^{-1})$	0.23 to 5112.32	163.81	42.14	0.23 to 5112.32	208.36	56.62	0.33 to 424.39	42.87	8.02
$\text{KP}_{out}(10^{38} \text{ erg s}^{-1})$	0.2 to 18166.25	602.86	62.1	0.24 to 18166.25	783.98	101.5	0.2 to 1425.12	111.26	34.4
$\dot{P}_{out}(10^{30} \text{ g cm s}^{-2})$	0.83 to 34222.09	1079.06	180.65	0.83 to 34222.09	1390.16	267.04	0.91 to 2761.69	234.64	60.19

Parameter	Total			Seyferts			LINERs		
	Range	Mean	Median	Range	Mean	Median	Range	Mean	Median
$V_{shift}(\text{km s}^{-1})$	−657.0 to 177.0	−278.0	−235.0	−657.0 to 177.0	−225.0	−185.0	−624.0 to −211.0	−526.0	−585.0
$\text{FWHM}_{out}(\text{km s}^{-1})$	172.0 to 1171.0	575.0	580.0	172.0 to 1151.0	545.0	536.0	580.0 to 1171.0	720.0	672.0
$V_{out}(\text{km s}^{-1})$	312.0 to 1387.0	777.0	733.0	312.0 to 1343.0	701.0	657.0	849.0 to 1387.0	1137.0	1136.0
AI	−0.51 to 0.16	−0.18	−0.17	−0.51 to 0.16	−0.15	−0.13	−0.44 to −0.01	−0.33	−0.37
$M_{out}(10^2 M_{\odot})$	0.3 to 1488.25	207.14	84.41	4.7 to 1488.25	233.8	94.93	0.3 to 616.59	79.95	33.35
$\dot{M}_{out}(10^{-3} M_{\odot} \text{ yr}^{-1})$	0.08 to 247.09	26.72	9.97	1.08 to 247.09	28.32	11.58	0.08 to 151.93	19.11	7.42
$\text{KP}_{out}(10^{38} \text{ erg s}^{-1})$	0.36 to 1053.8	63.07	14.99	0.46 to 1053.8	58.71	14.98	0.36 to 696.0	83.9	22.41
$\dot{P}_{out}(10^{30} \text{ g cm s}^{-2})$	0.58 to 1812.07	133.73	52.05	2.63 to 1812.07	132.02	55.32	0.58 to 1154.74	141.85	50.95

REFERENCES

- Aalto, S., Costagliola, F., Muller, S., et al. 2016, *A&A*, 590, A73, doi: [10.1051/0004-6361/201527664](https://doi.org/10.1051/0004-6361/201527664)
- Astropy Collaboration, Price-Whelan, A. M., Lim, P. L., et al. 2022, *ApJ*, 935, 167, doi: [10.3847/1538-4357/ac7c74](https://doi.org/10.3847/1538-4357/ac7c74)
- Audibert, A., Ramos Almeida, C., García-Burillo, S., et al. 2023, *A&A*, 671, L12, doi: [10.1051/0004-6361/202345964](https://doi.org/10.1051/0004-6361/202345964)
- Ayubinia, A., Woo, J.-H., Rakshit, S., & Son, D. 2023, *ApJ*, 954, 27, doi: [10.3847/1538-4357/ace0ba](https://doi.org/10.3847/1538-4357/ace0ba)
- Baldwin, J. A., Phillips, M. M., & Terlevich, R. 1981, *PASP*, 93, 5, doi: [10.1086/130766](https://doi.org/10.1086/130766)
- Baron, D., & Ménard, B. 2019, *MNRAS*, 487, 3404, doi: [10.1093/mnras/stz1546](https://doi.org/10.1093/mnras/stz1546)
- Becker, R. H., White, R. L., & Helfand, D. J. 1995, *ApJ*, 450, 559, doi: [10.1086/176166](https://doi.org/10.1086/176166)
- Belli, S., Park, M., Davies, R. L., et al. 2024, *Nature*, 630, 54, doi: [10.1038/s41586-024-07412-1](https://doi.org/10.1038/s41586-024-07412-1)
- Bischetti, M., Piconcelli, E., Feruglio, C., et al. 2019, *A&A*, 628, A118, doi: [10.1051/0004-6361/201935524](https://doi.org/10.1051/0004-6361/201935524)
- Bluck, A. F. L., Maiolino, R., Sánchez, S. F., et al. 2020, *MNRAS*, 492, 96, doi: [10.1093/mnras/stz3264](https://doi.org/10.1093/mnras/stz3264)
- Bruzual A., G. 1983, *ApJ*, 273, 105, doi: [10.1086/161352](https://doi.org/10.1086/161352)
- Bundy, K., Bershadsky, M. A., Law, D. R., et al. 2015, *ApJ*, 798, 7, doi: [10.1088/0004-637X/798/1/7](https://doi.org/10.1088/0004-637X/798/1/7)
- Caccianiga, A., Antón, S., Ballo, L., et al. 2015, *MNRAS*, 451, 1795, doi: [10.1093/mnras/stv939](https://doi.org/10.1093/mnras/stv939)
- Calzetti, D., Armus, L., Bohlin, R. C., et al. 2000, *ApJ*, 533, 682, doi: [10.1086/308692](https://doi.org/10.1086/308692)
- Cardelli, J. A., Clayton, G. C., & Mathis, J. S. 1989, *ApJ*, 345, 245, doi: [10.1086/167900](https://doi.org/10.1086/167900)
- Carniani, S., Venturi, G., Parlanti, E., et al. 2024, *A&A*, 685, A99, doi: [10.1051/0004-6361/202347230](https://doi.org/10.1051/0004-6361/202347230)
- Cattaneo, A., & Best, P. N. 2009, *MNRAS*, 395, 518, doi: [10.1111/j.1365-2966.2009.14557.x](https://doi.org/10.1111/j.1365-2966.2009.14557.x)
- Cavagnolo, K. W., McNamara, B. R., Nulsen, P. E. J., et al. 2010, *ApJ*, 720, 1066, doi: [10.1088/0004-637X/720/2/1066](https://doi.org/10.1088/0004-637X/720/2/1066)
- Condon, J. J., Cotton, W. D., & Broderick, J. J. 2002, *AJ*, 124, 675, doi: [10.1086/341650](https://doi.org/10.1086/341650)
- do Nascimento, J. C., Dors, O. L., Storchi-Bergmann, T., et al. 2022, *MNRAS*, 513, 807, doi: [10.1093/mnras/stac771](https://doi.org/10.1093/mnras/stac771)
- Dopita, M. A., & Sutherland, R. S. 1995, *ApJ*, 455, 468, doi: [10.1086/176596](https://doi.org/10.1086/176596)
- Elvis, M. 2000, *ApJ*, 545, 63, doi: [10.1086/317778](https://doi.org/10.1086/317778)
- Fabian, A. C. 2012, *ARA&A*, 50, 455, doi: [10.1146/annurev-astro-081811-125521](https://doi.org/10.1146/annurev-astro-081811-125521)
- Fernández-Ontiveros, J. A., Dasyra, K. M., Hatziminaoglou, E., et al. 2020, *A&A*, 633, A127, doi: [10.1051/0004-6361/201936552](https://doi.org/10.1051/0004-6361/201936552)
- Feruglio, C., Fiore, F., Carniani, S., et al. 2015, *A&A*, 583, A99, doi: [10.1051/0004-6361/201526020](https://doi.org/10.1051/0004-6361/201526020)
- Fiore, F., Feruglio, C., Shankar, F., et al. 2017, *A&A*, 601, A143, doi: [10.1051/0004-6361/201629478](https://doi.org/10.1051/0004-6361/201629478)
- Flesch, E. W. 2023, arXiv e-prints, arXiv:2308.01505, doi: [10.48550/arXiv.2308.01505](https://doi.org/10.48550/arXiv.2308.01505)
- García-Burillo, S., Combes, F., Usero, A., et al. 2014, *A&A*, 567, A125, doi: [10.1051/0004-6361/201423843](https://doi.org/10.1051/0004-6361/201423843)
- Girdhar, A., Harrison, C. M., Mainieri, V., et al. 2022, *MNRAS*, 512, 1608, doi: [10.1093/mnras/stac073](https://doi.org/10.1093/mnras/stac073)
- Greene, J. E., & Ho, L. C. 2005, *The Astrophysical Journal*, 630, 122, doi: [10.1086/431897](https://doi.org/10.1086/431897)
- Greene, J. E., & Ho, L. C. 2007, *ApJ*, 670, 92, doi: [10.1086/522082](https://doi.org/10.1086/522082)
- Guo, Y., Bacon, R., Bouché, N. F., et al. 2023, *Nature*, 624, 53, doi: [10.1038/s41586-023-06718-w](https://doi.org/10.1038/s41586-023-06718-w)
- Haidar, H., Rosario, D. J., Alonso-Herrero, A., et al. 2024, *MNRAS*, 532, 4645, doi: [10.1093/mnras/stae1596](https://doi.org/10.1093/mnras/stae1596)
- Harris, C. R., Millman, K. J., van der Walt, S. J., et al. 2020, *Nature*, 585, 357, doi: [10.1038/s41586-020-2649-2](https://doi.org/10.1038/s41586-020-2649-2)
- Harrison, C. M., Alexander, D. M., Mullaney, J. R., & Swinbank, A. M. 2014, *MNRAS*, 441, 3306, doi: [10.1093/mnras/stu515](https://doi.org/10.1093/mnras/stu515)
- Heckman, T. M. 1980, *A&A*, 87, 152
- Ho, L. C. 2008, *ARA&A*, 46, 475, doi: [10.1146/annurev.astro.45.051806.110546](https://doi.org/10.1146/annurev.astro.45.051806.110546)
- Hönig, S. F., Kishimoto, M., Tristram, K. R. W., et al. 2013, *ApJ*, 771, 87, doi: [10.1088/0004-637X/771/2/87](https://doi.org/10.1088/0004-637X/771/2/87)
- Hunter, J. D. 2007, *Computing In Science & Engineering*, 9, 90
- Husemann, B., Bennert, V. N., Jahnke, K., et al. 2019, *ApJ*, 879, 75, doi: [10.3847/1538-4357/ab24bc](https://doi.org/10.3847/1538-4357/ab24bc)
- Izumi, T., Wada, K., Imanishi, M., et al. 2023, *Science*, 382, 554, doi: [10.1126/science.adf0569](https://doi.org/10.1126/science.adf0569)
- Järvelä, E., Dahale, R., Crepaldi, L., et al. 2022, *A&A*, 658, A12, doi: [10.1051/0004-6361/202141698](https://doi.org/10.1051/0004-6361/202141698)
- Jarvis, M. E., Harrison, C. M., Thomson, A. P., et al. 2019, *MNRAS*, 485, 2710, doi: [10.1093/mnras/stz556](https://doi.org/10.1093/mnras/stz556)
- Kauffmann, G., Heckman, T. M., Tremonti, C., et al. 2003, *MNRAS*, 346, 1055, doi: [10.1111/j.1365-2966.2003.07154.x](https://doi.org/10.1111/j.1365-2966.2003.07154.x)
- Kelly, B. C. 2007, *ApJ*, 665, 1489, doi: [10.1086/519947](https://doi.org/10.1086/519947)
- Kennicutt, R. C., & Evans, N. J. 2012, *ARA&A*, 50, 531, doi: [10.1146/annurev-astro-081811-125610](https://doi.org/10.1146/annurev-astro-081811-125610)
- Kewley, L. J., Heisler, C. A., Dopita, M. A., & Lumsden, S. 2001, *ApJS*, 132, 37, doi: [10.1086/318944](https://doi.org/10.1086/318944)
- King, A., & Pounds, K. 2015, *ARA&A*, 53, 115, doi: [10.1146/annurev-astro-082214-122316](https://doi.org/10.1146/annurev-astro-082214-122316)

- Kozieł-Wierzbowska, D., Vale Asari, N., Stasińska, G., et al. 2021, *ApJ*, 910, 64, doi: [10.3847/1538-4357/abe308](https://doi.org/10.3847/1538-4357/abe308)
- Kukreti, P., Morganti, R., Tadhunter, C., & Santoro, F. 2023, *A&A*, 674, A198, doi: [10.1051/0004-6361/202245691](https://doi.org/10.1051/0004-6361/202245691)
- Law, D. R., Cherinka, B., Yan, R., et al. 2016, *AJ*, 152, 83, doi: [10.3847/0004-6256/152/4/83](https://doi.org/10.3847/0004-6256/152/4/83)
- Law, D. R., Belfiore, F., Bershad, M. A., et al. 2022, *ApJ*, 928, 58, doi: [10.3847/1538-4357/ac5620](https://doi.org/10.3847/1538-4357/ac5620)
- Liao, M., Wang, J., Ren, W., & Zhou, M. 2024, *MNRAS*, 528, 3696, doi: [10.1093/mnras/stae126](https://doi.org/10.1093/mnras/stae126)
- Luridiana, V., Morisset, C., & Shaw, R. A. 2015, *A&A*, 573, A42, doi: [10.1051/0004-6361/201323152](https://doi.org/10.1051/0004-6361/201323152)
- Lynden-Bell, D. 1969, *Nature*, 223, 690, doi: [10.1038/223690a0](https://doi.org/10.1038/223690a0)
- Márquez, I., Masegosa, J., González-Martin, O., et al. 2017, *Frontiers in Astronomy and Space Sciences*, 4, 34, doi: [10.3389/fspas.2017.00034](https://doi.org/10.3389/fspas.2017.00034)
- Martín-Navarro, I., Brodie, J. P., Romanowsky, A. J., Ruiz-Lara, T., & van de Ven, G. 2018, *Nature*, 553, 307, doi: [10.1038/nature24999](https://doi.org/10.1038/nature24999)
- Miller, J. S., & Mathews, W. G. 1972, *ApJ*, 172, 593, doi: [10.1086/151378](https://doi.org/10.1086/151378)
- Molyneux, S. J., Harrison, C. M., & Jarvis, M. E. 2019, *A&A*, 631, A132, doi: [10.1051/0004-6361/201936408](https://doi.org/10.1051/0004-6361/201936408)
- Morganti, R., Oosterloo, T., Oonk, J. B. R., Frieswijk, W., & Tadhunter, C. 2015, *A&A*, 580, A1, doi: [10.1051/0004-6361/201525860](https://doi.org/10.1051/0004-6361/201525860)
- Mullaney, J. R., Alexander, D. M., Fine, S., et al. 2013, *MNRAS*, 433, 622, doi: [10.1093/mnras/stt751](https://doi.org/10.1093/mnras/stt751)
- Murthy, S., Morganti, R., Wagner, A. Y., et al. 2022, *Nature Astronomy*, 6, 488, doi: [10.1038/s41550-021-01596-6](https://doi.org/10.1038/s41550-021-01596-6)
- Musiimenta, B., Brusa, M., Liu, T., et al. 2023, *A&A*, 679, A84, doi: [10.1051/0004-6361/202245555](https://doi.org/10.1051/0004-6361/202245555)
- Nandi, P., Stalin, C. S., Dam, P., & Saikia, D. J. 2024, *ApJ*, 973, 7, doi: [10.3847/1538-4357/ad5da9](https://doi.org/10.3847/1538-4357/ad5da9)
- Nandi, P., Stalin, C. S., Saikia, D. J., et al. 2023a, *ApJ*, 950, 81, doi: [10.3847/1538-4357/accf1e](https://doi.org/10.3847/1538-4357/accf1e)
- . 2023b, *ApJ*, 959, 116, doi: [10.3847/1538-4357/ad0c57](https://doi.org/10.3847/1538-4357/ad0c57)
- Osterbrock, D. E., & Ferland, G. J. 2006, *Astrophysics of gaseous nebulae and active galactic nuclei*
- Padovani, P. 2017, *Nature Astronomy*, 1, 0194, doi: [10.1038/s41550-017-0194](https://doi.org/10.1038/s41550-017-0194)
- Padovani, P., Alexander, D. M., Assef, R. J., et al. 2017, *A&A Rv*, 25, 2, doi: [10.1007/s00159-017-0102-9](https://doi.org/10.1007/s00159-017-0102-9)
- Panessa, F., Baldi, R. D., Laor, A., et al. 2019, *Nature Astronomy*, 3, 387, doi: [10.1038/s41550-019-0765-4](https://doi.org/10.1038/s41550-019-0765-4)
- Parlanti, E., Carniani, S., Venturi, G., et al. 2024, *arXiv e-prints*, arXiv:2407.19008, doi: [10.48550/arXiv.2407.19008](https://doi.org/10.48550/arXiv.2407.19008)
- Paulino-Afonso, A., Sobral, D., Darvish, B., et al. 2020, *A&A*, 633, A70, doi: [10.1051/0004-6361/201834244](https://doi.org/10.1051/0004-6361/201834244)
- Ramos Almeida, C., Bischetti, M., García-Burillo, S., et al. 2022, *A&A*, 658, A155, doi: [10.1051/0004-6361/202141906](https://doi.org/10.1051/0004-6361/202141906)
- Reines, A. E. 2022, *Nature Astronomy*, 6, 26, doi: [10.1038/s41550-021-01556-0](https://doi.org/10.1038/s41550-021-01556-0)
- Riffel, R. A., Storchi-Bergmann, T., Riffel, R., et al. 2023, *MNRAS*, 521, 1832, doi: [10.1093/mnras/stad599](https://doi.org/10.1093/mnras/stad599)
- Sabater, J., Best, P. N., Hardcastle, M. J., et al. 2019, *A&A*, 622, A17, doi: [10.1051/0004-6361/201833883](https://doi.org/10.1051/0004-6361/201833883)
- Saikia, D. J. 2022, *Journal of Astrophysics and Astronomy*, 43, 97, doi: [10.1007/s12036-022-09863-2](https://doi.org/10.1007/s12036-022-09863-2)
- Salem, N., Masters, K. L., Stark, D. V., & Sharma, A. 2024, *Research Notes of the American Astronomical Society*, 8, 188, doi: [10.3847/2515-5172/ad676f](https://doi.org/10.3847/2515-5172/ad676f)
- Sánchez, S. F., Barrera-Ballesteros, J. K., Lacerda, E., et al. 2022, *ApJS*, 262, 36, doi: [10.3847/1538-4365/ac7b8f](https://doi.org/10.3847/1538-4365/ac7b8f)
- Speranza, G., Ramos Almeida, C., Acosta-Pulido, J. A., et al. 2022, *A&A*, 665, A55, doi: [10.1051/0004-6361/202243585](https://doi.org/10.1051/0004-6361/202243585)
- Spindler, A., Wake, D., Belfiore, F., et al. 2018, *MNRAS*, 476, 580, doi: [10.1093/mnras/sty247](https://doi.org/10.1093/mnras/sty247)
- Stalevski, M., Tristram, K. R. W., & Asmus, D. 2019, *MNRAS*, 484, 3334, doi: [10.1093/mnras/stz220](https://doi.org/10.1093/mnras/stz220)
- Su, R., Mahony, E. K., Gu, M., et al. 2023, *MNRAS*, 520, 5712, doi: [10.1093/mnras/stad370](https://doi.org/10.1093/mnras/stad370)
- Tadhunter, C. 2016, *A&A Rv*, 24, 10, doi: [10.1007/s00159-016-0094-x](https://doi.org/10.1007/s00159-016-0094-x)
- Taylor, M. B. 2005, in *Astronomical Society of the Pacific Conference Series*, Vol. 347, *Astronomical Data Analysis Software and Systems XIV*, ed. P. Shopbell, M. Britton, & R. Ebert, 29
- Torres-Papaqui, J. P., Coziol, R., Robledo-Orús, A. C., Cutiva-Alvarez, K. A., & Roco-Avilez, P. 2024, *AJ*, 168, 37, doi: [10.3847/1538-3881/ad43db](https://doi.org/10.3847/1538-3881/ad43db)
- Veilleux, S., Kim, D. C., Sanders, D. B., Mazzarella, J. M., & Soifer, B. T. 1995, *ApJS*, 98, 171, doi: [10.1086/192158](https://doi.org/10.1086/192158)
- Venturi, G., Cresci, G., Marconi, A., et al. 2021, *A&A*, 648, A17, doi: [10.1051/0004-6361/202039869](https://doi.org/10.1051/0004-6361/202039869)
- Venturi, G., Treister, E., Finlez, C., et al. 2023, *A&A*, 678, A127, doi: [10.1051/0004-6361/202347375](https://doi.org/10.1051/0004-6361/202347375)
- Virtanen, P., Gommers, R., Oliphant, T. E., et al. 2020, *Nature Methods*, 17, 261, doi: [10.1038/s41592-019-0686-2](https://doi.org/10.1038/s41592-019-0686-2)
- Wake, D. A., Bundy, K., Diamond-Stanic, A. M., et al. 2017, *AJ*, 154, 86, doi: [10.3847/1538-3881/aa7ecc](https://doi.org/10.3847/1538-3881/aa7ecc)

- Westfall, K. B., Cappellari, M., Bershady, M. A., et al. 2019, *AJ*, 158, 231, doi: [10.3847/1538-3881/ab44a2](https://doi.org/10.3847/1538-3881/ab44a2)
- Wilkins, S. M., Lovell, C. C., Irodotou, D., et al. 2024, *MNRAS*, 527, 7965, doi: [10.1093/mnras/stad3558](https://doi.org/10.1093/mnras/stad3558)
- Woo, J.-H., Bae, H.-J., Son, D., & Karouzos, M. 2016, *ApJ*, 817, 108, doi: [10.3847/0004-637X/817/2/108](https://doi.org/10.3847/0004-637X/817/2/108)
- Wright, E. L., Eisenhardt, P. R. M., Mainzer, A. K., et al. 2010, *AJ*, 140, 1868, doi: [10.1088/0004-6256/140/6/1868](https://doi.org/10.1088/0004-6256/140/6/1868)
- Wylezalek, D., & Morganti, R. 2018, *Nature Astronomy*, 2, 181, doi: [10.1038/s41550-018-0409-0](https://doi.org/10.1038/s41550-018-0409-0)
- Zakamska, N. L., & Greene, J. E. 2014, *MNRAS*, 442, 784, doi: [10.1093/mnras/stu842](https://doi.org/10.1093/mnras/stu842)
- Zamanov, R., Marziani, P., Sulentic, J. W., et al. 2002, *ApJL*, 576, L9, doi: [10.1086/342783](https://doi.org/10.1086/342783)
- Zhang, K., Wang, T.-G., Yan, L., & Dong, X.-B. 2013, *ApJ*, 768, 22, doi: [10.1088/0004-637X/768/1/22](https://doi.org/10.1088/0004-637X/768/1/22)
- Zhuang, M.-Y., & Ho, L. C. 2023, *Nature Astronomy*, 7, 1376, doi: [10.1038/s41550-023-02051-4](https://doi.org/10.1038/s41550-023-02051-4)